

1 Carbon export and burial pathways driven by a low-latitude arc- 2 continent collision

3 Amy I. Hsieh¹, Thierry Adatte¹, Shraddha Band², Li Lo³, Romain Vaucher⁴, Brahim Samba Bomou¹,
4 Laszlo Kocsis⁵, Pei-Ling Wang⁶, Samuel Jaccard¹

5 ¹Institute of Earth Sciences, University of Lausanne, Lausanne, CH-1015, Switzerland

6 ²Biodiversity Research Center, Academia Sinica, Taipei, 115, Taiwan

7 ³Department of Geosciences, National Taiwan University, Taipei, 106, Taiwan

8 ⁴College of Science and Engineering, James Cook University, Townsville, 4814, Australia

9 ⁵Institute of Earth Surface Dynamics, University of Lausanne, Lausanne, CH-1015, Switzerland

10 ⁶Institute of Oceanography, National Taiwan University, Taipei, 106, Taiwan

11 *Correspondence to:* Amy I. Hsieh (hsiehiamy@gmail.com)

12 **Abstract.** Chemical weathering of silicate rocks of low-latitude arc–continent collisions has been hypothesized as a driver of
13 global cooling since the Neogene. In mid- to low-latitude regions, monsoon and tropical cyclone precipitation also drive
14 intense physical erosion that contribute to terrestrial carbon export and nutrient-stimulated marine productivity. Despite this,
15 the role of physical erosion on carbon sequestration has largely been overlooked. To address this gap, we analyse late
16 Miocene–early Pleistocene sedimentary and geochemical records from the Taiwan Western Foreland Basin and time-
17 equivalent records from the northern South China Sea.

18 Along the continental slope, organic carbon accumulation is largely controlled by long-term sea-level fall and shoreline
19 progradation. In contrast, on the continental rise, organic carbon burial is controlled by high sedimentation rates related to
20 Taiwan’s uplift and erosion (since ~5.4 Ma). Despite increased terrestrial erosion of Taiwan, the organic material remains
21 mainly marine in origin, suggesting that primary production was enhanced along the coast by nutrient exported from Taiwan.
22 Marine organic matter along Taiwan’s shore was subsequently remobilized by turbidity currents through submarine canyon
23 systems and accumulating on the continental rise of Eurasia. The onset of Northern Hemisphere Glaciation (~3 Ma) and
24 subsequent intensification of the East Asian Summer Monsoon during interglacial periods, and persistent tropical cyclone
25 activity all further amplified nutrient export across the basin, further stimulating marine primary production.

26 Our findings demonstrate that arc–continent collision influences carbon sequestration through two pathways: (1) direct burial
27 of terrestrial organic matter and (2) nutrient-fuelled marine productivity and burial. This work establishes a direct link
28 between the erosion of an arc-continent collision and long-term carbon burial in adjacent ocean basins.

29 1 Introduction

30 Global cooling since the late Eocene has traditionally been attributed to tectonic forcing and enhanced chemical weathering
31 of silicate rock from the Himalayan and Tibetan Plateau (Raymo and Ruddiman, 1992), which results in the removal of

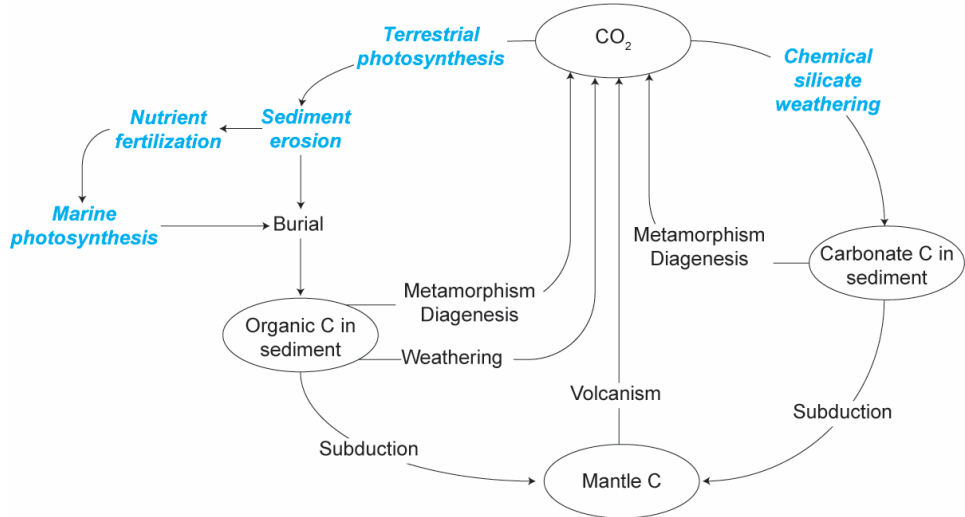
32 atmospheric CO₂ (Walker et al., 1981). However, weathering fluxes have decreased in both regions during the Neogene
33 (Clift and Jonell, 2021; Clift et al., 2024a), and global silicate fluxes appear to have remained near steady-state through the
34 Cenozoic (Caves et al., 2016) even as global cooling continued. To reconcile stable or declining chemical weathering rates
35 with decreasing atmospheric CO₂, an alternative hypothesis emphasized chemical erosion of arc-continent collisional
36 orogens in low-latitude, tropical regions (Clift et al., 2024b; Jagoutz et al., 2016; Macdonald et al., 2019; Bayon et al., 2023).
37 In such environments, warm and humid conditions amplify chemical weathering, enhancing carbon removal and
38 sequestration. While existing studies support a correlation between the growth and weathering of low-latitude orogens and
39 long-term atmospheric CO₂ concentration and global temperature records, they have yet to fully account for the roles of
40 physical erosion, terrestrial organic carbon burial, and changes in marine productivity.

41 In low-latitude regions, tropical cyclones and monsoons are the primary drivers of erosion and sediment dispersal, delivering
42 elevated sediment loads to adjacent seas via intense precipitation and high river discharge from steep mountainous
43 catchments (Chen et al., 2018; Milliman and Kao, 2005). Warm sea-surface temperatures and reduced polar ice volumes
44 under greenhouse climates would likely amplify monsoon variability and produce frequent and intense tropical cyclones
45 (Fedorov et al., 2013). These conditions of elevated humidity and precipitation would have promoted not only enhanced
46 chemical weathering of silicate rocks, but also greater terrestrial biomass production.

47 Land-to-sea export of terrestrial organic material from vegetation, soil, and rock is enhanced under high precipitation
48 regimes, with steep mountain rivers efficiently transporting this material for burial in adjacent ocean basins (Milliman et al.,
49 2017; Hilton et al., 2011). The global terrestrial carbon pool accounts for ~7.5% of the Earth's total carbon stock, excluding
50 lithospheric carbon, and is more than five times larger than the atmospheric carbon pool (Canadell et al., 2021). As a result,
51 even modest changes in the terrestrial carbon storage can significantly alter atmospheric CO₂ concentrations (Houghton,
52 2003). In particular, physical erosion by water is widely recognized as a dominant control of land-atmosphere carbon
53 exchange (Hilton and West, 2020; Van Oost et al., 2012). Elevated sediment discharge to the oceans would facilitate the
54 export and burial of terrestrial organic carbon (Galy et al., 2007; Hilton et al., 2011; Liu et al., 2013; Aumont et al., 2001;
55 Dagg et al., 2004; Jin et al., 2023), and also deliver bioessential nutrients that stimulate marine productivity (Hoshiba and
56 Yamanaka, 2013; Krumins et al., 2013; Dürr et al., 2011; Beusen et al., 2016). However, the role of fluvial nutrient export in
57 fuelling marine primary productivity is generally thought to be limited to coastal regions (Froelich, 1988; Stepanauskas et
58 al., 2002; Dagg et al., 2004). This oversimplification in ocean biogeochemical models leads to a poorly constrained link
59 between terrestrial nutrient supply, open-ocean productivity, and deep-sea carbon burial.

60 This research aims to address these knowledge gaps by disentangling the different mechanisms through which carbon is
61 sequestered as a result of low-latitude arc-continent collisions (Figure 1). A clearer understanding of these processes will
62 provide stronger constraints on both reconstructed and predictive carbon budget models. The study area focuses on the
63 northern South China Sea (SCS) region, specifically late Miocene to early Pleistocene (~6.3–2 Ma) strata of the Taiwan
64 Western Foreland Basin (TWFB, i.e., paleo-Taiwan Strait; Figure 2) and time-equivalent sediment core records obtained
65 from the Ocean Drilling Program (ODP Sites 1146 and 1148; Figure 2). Since its emergence in the early Pliocene, Taiwan

66 has been characterized by exceptionally high denudation rates and rapidly became the dominant sediment source to the
 67 adjacent TWFB, overwhelming contributions from southeast Eurasia (Hsieh et al., 2023b). Hyperpycnal flows triggered by
 68 intense precipitation transported Taiwan-derived sediments over 1000 km into the SCS, leaving a distinct signature in deep-
 69 sea deposits (Hsieh et al., 2024; Liu et al., 2012). Strata of the TWFB capture the evolution of the Taiwan Orogen (Lin and
 70 Watts, 2002), and thus provide insight into how changes in weathering and erosion processes modulated carbon burial in the
 71 SCS sediments across successive orogenesis stages.

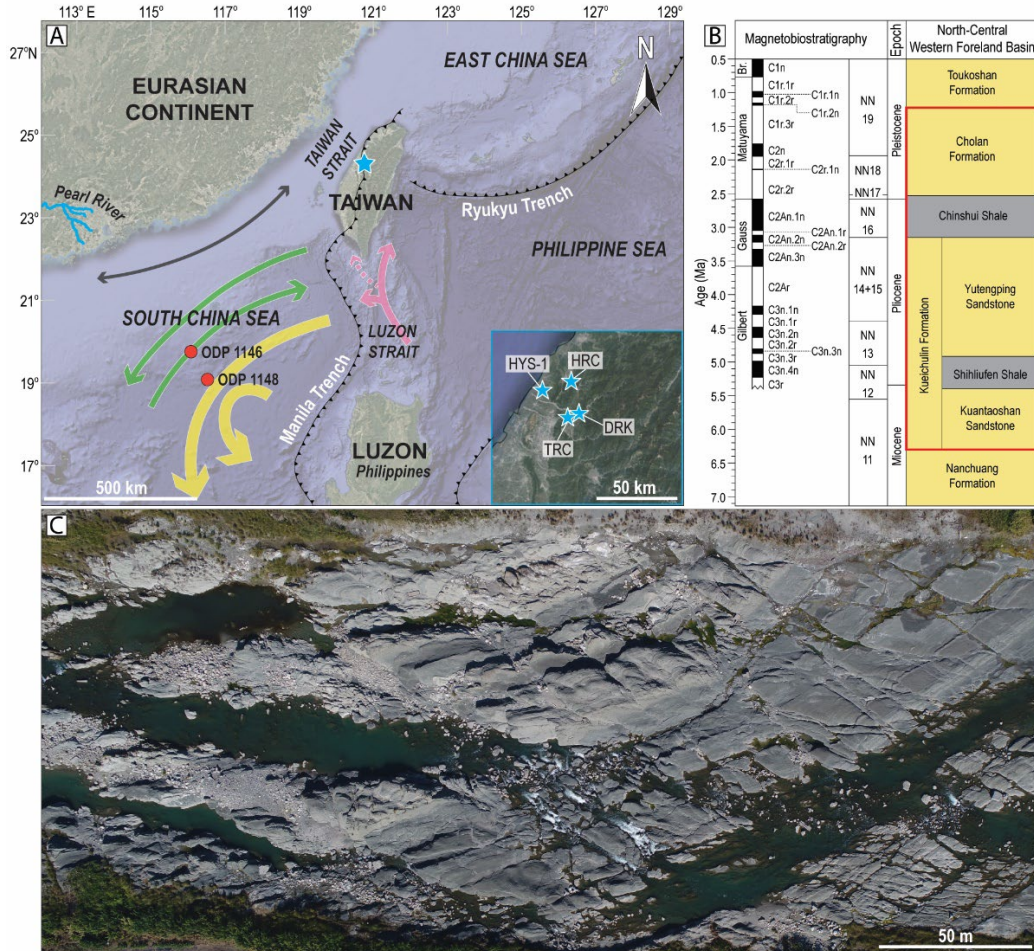


72
 73 **Figure 1: Conceptual model of geologic carbon (C) sources and sinks, modified from (Berner, 2003).** This research focuses on two
 74 main pathways of carbon sequestration often associated with arc-continent collisions, highlighted in blue: (1) direct burial of
 75 terrestrial organic matter, and (2) nutrient-fuelled marine productivity followed by the burial of marine organic matter. These
 76 processes play a crucial role in the long-term carbon cycle and the regulation of atmospheric CO₂.

77 2 Study area

78 The base of the TWFB stratigraphic fill is composed of the Kueichulin Formation, a sandstone-dominated unit deposited
 79 between the late Miocene–early Pliocene in shallow-marine and deltaic environments under the influence of wave and tidal
 80 processes, and composed of three members (from base to top): the Kuantaoshan Sandstone, Shihliufen Shale, and
 81 Yutengping Sandstone (Figure 2; Castelltort et al., 2011; Nagel et al., 2013; Hsieh et al., 2025). Overlying the Kueichulin
 82 Formation is the Chinshui Shale, a mudstone-rich succession deposited in the late Pliocene with uncommon wavy-laminated
 83 sandstone interbeds that accumulated in an offshore setting during a phase of maximum flooding and enhanced subsidence in
 84 the TWFB (Castelltort et al., 2011; Nagel et al., 2013; Pan et al., 2015). The Chinshui Shale is overlain by the Cholan
 85 Formation during the early Pleistocene, which consists of heterolithic sediments deposited in shallow-marine environments
 86 influenced by waves, rivers, and tides (Covey, 1986; Nagel et al., 2013; Pan et al., 2015; Vaucher et al., 2023a).
 87 The time interval between ~6.27–1.95 Ma was targeted because it spans the initiation of Taiwan’s emergence and uplift by
 88 the ongoing Eurasian-Philippine plate collision. It also includes the Pliocene (5.33–2.58 Ma), which may be the most recent

89 time in Earth's history when atmospheric CO₂ last reached or exceeded present-day concentrations (>400 ppm; Tierney et
90 al., 2019), and the subsequent transition toward Pleistocene icehouse conditions. Additionally, since tectonic configurations,
91 insolation, and major floral and faunal assemblages have remained broadly unchanged since the mid-Pliocene (Dowsett,
92 2007; Robinson et al., 2008), this period also provides a critical Earth system analogue for evaluating future climate hazards
93 (e.g., Burke et al., 2018), including sea-level rise and extreme weather events.



94

95 **Figure 2: A)** Map of the study area showing the locations of the Late Miocene–Early Pleistocene records from Ocean Drilling
96 Program (ODP) sediment cores (orange circles) in the South China Sea, and outcrop locations from the Taiwan Western Foreland
97 Basin (TWFB) (blue stars). The inset map outlined in blue show the locations of the borehole (HYS-1) and outcrop locations (DRK
98 = Da'an River, Kueichulin Formation; TRC = Tachia River, Chinshui Shale; HRC = Houlong River, Cholan Formation) of the
99 TWFB strata used in this study. Modern-day circulation in the SCS is shown in arrows: black = alongshore surface current, green
100 = surface- and intermediate-water currents, yellow = deep- and bottom-water current, pink = Kuroshio current, pink (dashed) =
101 Taiwan warm current (modified from Hu et al. (2010); Liu et al. (2010a); Liu et al. (2016); Yin et al. (2023)). **B)** Chronostratigraphy
102 of the TWFB is modified after Chen (2016), Hsieh et al. (2023a), and Teng et al. (1991). The red box highlights
103 the targeted study section. Yellow denotes sandstone-dominated strata, and grey indicates mudstone-dominated strata. **C)** Outcrop
104 photo of the Chinshui Shale at Tachia River (this study).

105 **3 Methodology**106 **3.1 Data acquisition and analysis**

107 A total of 553 samples were collected from outcrops of the TWFB exposed along rivers in southwestern Taiwan, including
108 272 collected from the Kueichulin Formation by Dashtgard et al. (2021) and Hsieh et al. (2023b) along the Da'an River
109 (Figure 2A). This was combined with new data from the Chinshui Shale (n=90; Tachia River) and the Cholan Formation
110 (n=191; Houlong River) (Figure 2A). Data between 4.13–3.15 Ma are not available as no outcrop sections were accessible.
111 Gamma-ray data were obtained from the HYS-1 borehole drilled through the TWFB. Age-equivalent material was also
112 obtained from deep-sea sediment cores ODP Site 1146 (19°27.40'N, 116°16.37'E, 2092 m water depth, 179.8–343.1 m core
113 depth; Holbourn et al., 2005; Holbourn et al., 2007) and Site 1148 (18°50.169'N, 116°33.939'E, 3294 m water depth, 118.9–
114 206 m core depth; Tian et al., 2008; Cheng et al., 2004), archived in international core repositories. Sampling resolution
115 averaged ~1.4 m vertically through the TWFB stratigraphic sections, and ~0.65 m and ~0.35 m through the ODP Sites 1146
116 and 1148 cores, respectively.

117 Samples from the Chinshui Shale and ODP sites were analysed for organic geochemistry and paleomagnetism. For the
118 Chinshui Shale, total organic carbon (TOC) and total nitrogen (TN) concentrations were determined from pulverized rock
119 samples in the Department of Geosciences at National Taiwan University (NTU) using an elemental analyser (Elementar
120 TOC analyser soli TOC® cube; Lin et al., 2025). Total carbon (TC) and TN abundances for ODP samples were determined
121 with a CHNS Elemental Analyser (Thermo Finnigan Flash EA 1112) at the Institute of Earth Sciences (ISTE) at the
122 University of Lausanne in Switzerland on oven-dried sieved and crushed sediment samples. The samples were heated to
123 900°C, after which the combustion products were extracted into a chromatographic column where they were converted into
124 simpler components: CO₂ and N₂. These components were then measured by a thermal conductivity detector, and the results
125 were expressed as a weight percentage. Analytical precision and accuracy were determined by replicate analyses and by
126 comparison with an organic analytical standard composed of purified L-cysteine, achieving a precision of better than 0.3%.
127 Organic matter (OM) analyses of ODP core samples were performed on whole-rock powdered samples using a Rock-Eval 6
128 at the ISTE following the method described by Espitalie et al. (1985) and Behar et al. (2001). Measurements were calibrated
129 using the IFP 160000 standard. Rock-Eval pyrolysis provides parameters such as hydrogen index (HI, mg HC g⁻¹ TOC, HC
130 = hydrocarbons), oxygen index (OI, mg CO₂ g⁻¹ TOC), *T_{max}* (°C), and the TOC (wt.%). HI, OI and *T_{max}* values, which give an
131 overall measure of the type and maturation of the organic matter (e.g., Espitalie et al., 1985), can't be interpreted for TOC <
132 0.2 wt.% and *S₂* values ≥ 0.2 mg HC g⁻¹. Total organic carbon accumulation rates (mg cm⁻² kyr⁻¹) for the ODP sites were
133 calculated by multiplying mass-accumulation rates (MAR) derived from literature and TOC.
134 Organic carbon isotopic compositions ($\delta^{13}\text{C}_{\text{org}}$, ‰ relative to Vienna Pee Dee Belemnite) were measured by flash
135 combustion on an elemental analyser (EA) coupled to an isotope-ratio mass spectrometer (IRMS) from pulverized,
136 decarbonated (10% HCl treatment) whole-rock samples. Samples from ODP sites were analysed at the Institute of Earth
137 Surface Dynamics, University of Lausanne, using a Thermo EA IsoLink CN connected to a Delta V Plus isotope ratio mass

138 spectrometer (Thermo Fisher Scientific, Bremen), both operated under continuous helium flow. The samples and standards
139 are weighed in tin capsules and combusted at 1020°C with oxygen pulse in a quartz reactor filled with chromium oxide
140 (Cr_2O_3) and below with silvered cobaltous-cobaltic oxide. The combustion produced gases (CO_2 , N_2 , NO_x and H_2O) are
141 carried by the He-flow to a second reactor filled with elemental copper and copper oxide wires kept at 640°C to remove
142 excess oxygen and reduce non-stoichiometric nitrous products to N_2 . The gases are then carried through a water trap filled
143 with magnesium perchlorate ($\text{Mg}(\text{ClO}_4)_2$). The dried N_2 and CO_2 gases are separated with a gas chromatograph column at 70
144 °C and then carried to the mass spectrometer. The measured $\delta^{13}\text{C}$ values are calibrated and normalized using international
145 reference materials and in-house standards Spangenberg, 2016. Samples from the Chinshui Shale were analysed at the Stable
146 Isotope Laboratory at National Taiwan University using a Flash EA (Thermo Fisher Scientific) coupled to a Delta V
147 Advantage (Thermo Fisher Scientific). The $\delta^{13}\text{C}$ values are calibrated using an international reference material, IAEA-CH-3.
148 The reproducibility and accuracy are better than $\pm 0.1\text{\textperthousand}$.

149 Thirty-three oriented palaeomagnetic core specimens (25-mm diameter) were collected at ~ 3.5 m intervals from
150 unweathered, mud-rich beds from the Chinshui Shale, then prepared and analysed at Academia Sinica in Taiwan following
151 the methodology described in Horng (2014). Cores were cut into 2-cm samples, and bulk magnetic susceptibility measured
152 using a Bartington Instruments MS2B magnetic susceptibility meter. Mass-specific magnetic susceptibility (χ) was then
153 derived by normalising bulk magnetic susceptibility to sample mass.

154 Existing data for the ODP sites 1146 and 1148 were also compiled from literature, including clastic MAR (Site 1146 from
155 Wan et al., 2010a, Site 1148 from Wang et al., 2000a), magnetic susceptibility (1146 from Wang et al., 2005a, 1148 from
156 Wang et al., 2000a), hematite/goethite ratios (Hm/Gt) derived from spectral reflectance band ratios at 565/435 nm (1146
157 from Wang et al., 2000b, 1148 from Clift, 2006), continuous gamma-ray logs (1146 from Wang et al., 2000b, 1148 from
158 Wang et al., 2000a), and titanium/calcium ratios (Ti/Ca ; 1146 from Wan et al., 2010a, 1148 from Hoang et al., 2010).
159 Magnetic susceptibility and Ti/Ca serve as proxies for physical erosion, recording variations in terrigenous sediment flux
160 linked to summer monsoon precipitation. Intensified precipitation enhances basin sediment accumulation rates (Clift et al.,
161 2014), and typically increases the magnetic susceptibility of marine sediment via enhanced runoff and terrestrial input (Clift
162 et al., 2002; Kissel et al., 2017; Tian et al., 2005). In the SCS, magnetic susceptibility also serves as a sediment provenance
163 indicator. Along the Taiwan Strait, sediment sourced from western Taiwan yields χ values that range from 0.9 ± 0.3 to $1.8 \pm$
164 $0.5 \times 10^{-7} \text{ m}^3 \text{ kg}^{-1}$, much lower than those sourced from the South China Block ($4.0 \pm 1.3 \times 10^{-7} \text{ m}^3 \text{ kg}^{-1}$), indicating a relative
165 depletion of magnetic minerals in Taiwan-sourced material (Horng and Huh, 2011). Titanium, associated with heavy mineral
166 deposition, and calcium, linked to pelagic biogenic carbonate accumulation, yield Ti/Ca values that increase with enhanced
167 monsoon-driven sediment export (Clift et al., 2014). Gamma-ray intensities broadly track changes in lithology (Green and
168 Fearon, 1940; Schlumberger, 1989), where values < 75 American Petroleum Institute (API) typically mark sandstone-rich
169 intervals, > 105 API mudstone-rich intervals, and intermediate values reflect mixed lithologies. Increased sediment export,
170 particularly of coarser grains, may be expressed as lower API values.

171 Sedimentary TOC content provides a measure of organic carbon accumulation through time. Terrestrial and marine sources
 172 can also be differentiated by their $\delta^{13}\text{C}_{\text{org}}$ values (Dashtgard et al., 2021; Hilton et al., 2010; Chmura and Aharon, 1995;
 173 Peterson and Fry, 1987; Martiny et al., 2013). Marine organic matter (e.g., plankton, particulate and dissolved organic
 174 matter) typically have more enriched values than terrestrial inputs (e.g., C3 and C4 plants, and soil and lithogenic organic
 175 carbon) (Table 1). Marine-derived organic matter mainly accumulates on the seafloor under fair-weather conditions, while
 176 terrestrial input increases under intervals of increased precipitation and erosion (Hsieh et al., 2023b; Dashtgard et al., 2021).

177 **Table 1: Typical values for marine- and terrestrially sourced $\delta^{13}\text{C}_{\text{org}}$ and C/N (compiled by Dashtgard et al., 2021). Numbers in**
 178 **brackets represent sample count. OM = organic material.**

| | Organic Material | $\delta^{13}\text{C}_{\text{org}} (\text{‰})$ | C/N |
|-------------|--|---|---------------------|
| Marine | Particulate OM | -22.5 ± 1.7 (53) | 6.2 ± 1.0 |
| | Plankton | -20.4 ± 1.4 (184) | - |
| | Dissolved OM | -22.5 ± 0.8 (23) | - |
| Terrestrial | All pelagic marine organic matter - equally weighted | -21.8 ± 1.7 | 6.2 ± 1.0 |
| | High- ^{13}C plants (C4) | -13.2 ± 1.9 (89) | 83.3 ± 54 (6) |
| | Low- ^{13}C plants (C3) | -27.4 ± 1.9 (161) | 52 ± 14.8 (55) |
| | Soil | -25.9 ± 1.2 (11) | 17.1 ± 7.3 (22) |

179

180 Hematite-to-goethite (Hm/Gt) ratios are widely applied as indicator of monsoon precipitation (Clift, 2006; Liu et al., 2007;
 181 Zhang et al., 2009). Hematite typically forms through iron oxidation under arid climates or seasonal climates with dry
 182 seasons, whereas goethite preferentially develops under humid climates (e.g., Kämpf and Schwertmann, 1983; Maher, 1986).
 183 In the northern SCS, however, Clift et al. (2014) documented a positive relationship between elevated Hm/Gt values and
 184 intensified East Asian Summer Monsoon (EASM) rainfall and seasonality. Beyond climate, hematite also reflects sediment
 185 provenance: sediment derived from Taiwan is notably depleted in hematite and enriched in pyrrhotite (Horng and Huh,
 186 2011). Locally estimated scatterplot smoothing (LOESS) is applied to all data to reveal trends through the studied time
 187 interval (Cleveland et al., 1992).

188 3.2 Age models

189 The chronostratigraphic framework for the Kueichulin Formation, Chinshui Shale, and Cholan Formation of the TWFB was
 190 established by astronomically tuning the gamma-ray records to the $\delta^{18}\text{O}$ record of Wilkens et al. (2017) (Hsieh et al., 2023a;
 191 Vaucher et al., 2023b). However, the boundary between the top of the Kueichulin Formation and the base of the Chinshui

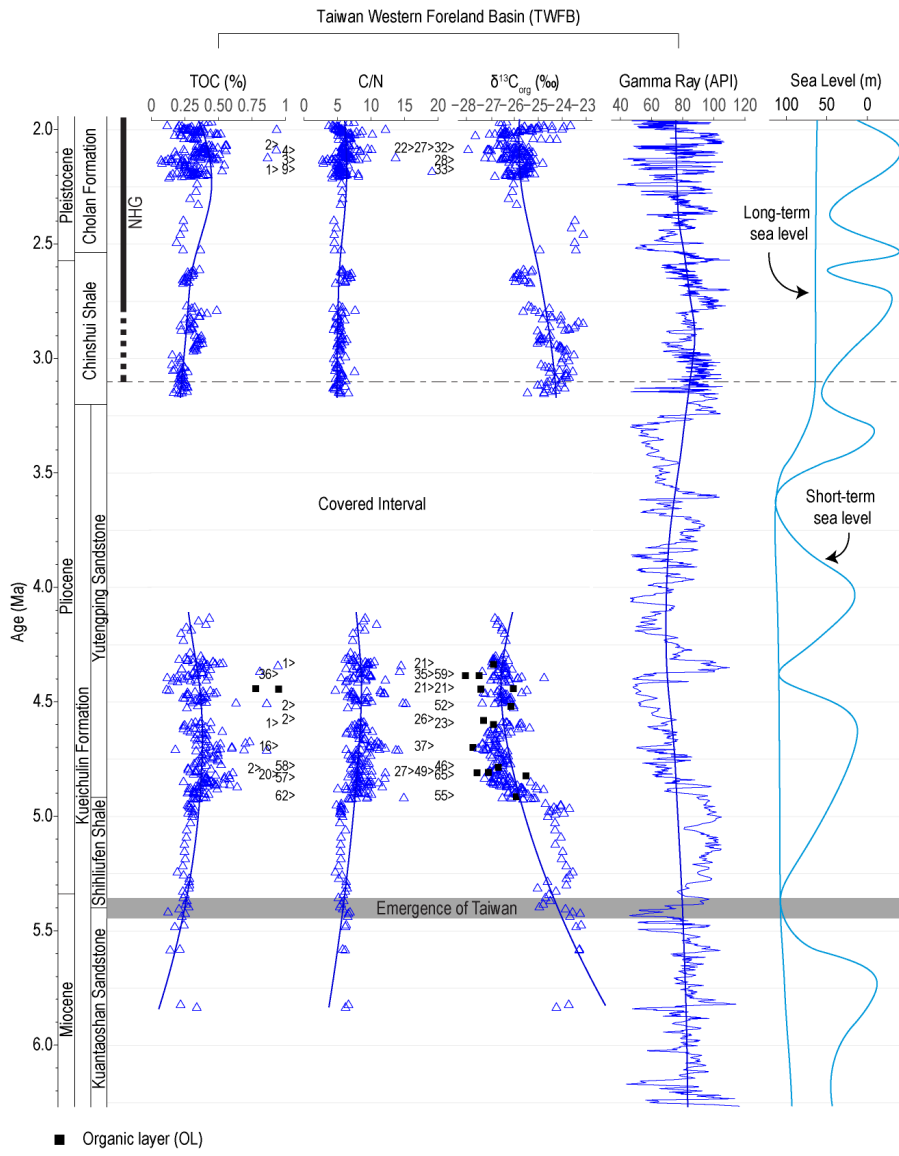
192 Shale is not well-established. Therefore, a magnetobiostratigraphic age model was developed from nannofossil zones and
193 magnetic reversals identified in oriented outcrop core samples from the Chinshui Shale outcrop using the methodology
194 described in Horng (2014) to ground-truth the existing framework. The remanent magnetic intensity, and declination and
195 inclination of oriented core samples were measured using a JR-6A spinner magnetometer (AGICO). To determine the stable
196 remanent magnetization and polarity (i.e., normal or reversed) of each sample, unstable secondary magnetization was
197 removed by thermally demagnetizing the samples stepwise from 25 to 600°C. The characteristic remanent magnetization
198 (ChRM) declination and inclination of thermally demagnetized samples were calculated using principal component analysis
199 with a minimum of three demagnetization steps in the PuffinPlot software (Lurcock and Wilson, 2012) to determine the
200 polarity of each sample. Thermal demagnetization diagrams for the Chinshui Shale samples showing the stable remanent
201 magnetic declinations and inclinations after principal component analysis are presented in Figure S1 in Supporting
202 Information.

203 Index nannofossils and corresponding biozonations identified by Shea and Huang (2003) for the Chinshui Shale were used to
204 constrain paleomagnetic polarities. The resulting age model was then correlated to an orbitally tuned, benthic foraminiferal,
205 stable oxygen isotope ($\delta^{18}\text{O}$) record from the equatorial Atlantic Ocean (Wilkens et al., 2017), which is tied to physical
206 sedimentary properties independent of ice volume, and has a robust timescale. Variations in both parameters are assumed to
207 be causally linked and temporally in-phase.

208 The age model for ODP Site 1146 (Wan et al., 2010a) was constructed by linear interpolation between
209 magnetobiostratigraphic age control points established by Wang et al. (2000b). Stratigraphic ages from ODP Site 1148 are
210 constrained using biostratigraphic ages of benthic foraminifera (Wang et al., 2000a).

211 **4 Results**

212 Data collected from the Chinshui Shale ($n = 90$) for this study have average TOC values ($0.3 \pm 0.1\%$) comparable to those of
213 the Shihliufen Shale ($0.3 \pm 0.03\%$, $n = 31$), but are higher than the basal Kuantaoshan Sandstone ($0.2 \pm 0.1\%$, $n = 9$), and
214 lower than the Yutengping Sandstone ($0.4 \pm 0.1\%$, $n = 216$) and the Cholan Formation ($0.4 \pm 0.7\%$, $n = 191$; Figure 3). C/N
215 and $\delta^{13}\text{C}_{\text{org}}$ values of the Chinshui Shale (5.2 ± 0.7 and $-24.5 \pm 0.7\text{‰}$, respectively) indicate stable accumulation of marine
216 organic content, similar to the Shihliufen Shale (5.3 ± 0.4 and $-24.2 \pm 0.4\text{‰}$) in contrast to the Kuantaoshan Sandstone ($6.1 \pm$
217 0.3 , $-23.4 \pm 0.3\text{‰}$), Yutengping Sandstone (8.5 ± 1.8 , $-26.5 \pm 0.5\text{‰}$), as well as the overlying Cholan Formation (6.3 ± 4.1 ,
218 $-25.7 \pm 0.8\text{‰}$), which records enhanced terrestrial input (Figure 3). The accumulation of marine organic matter is also stable
219 through the Shihliufen Shale and the Chinshui shale, with greater variability between ~ 4.9 – 4 Ma (Yutengping Sandstone),
220 and after ~ 2.3 Ma (Cholan Formation; Figure 3).



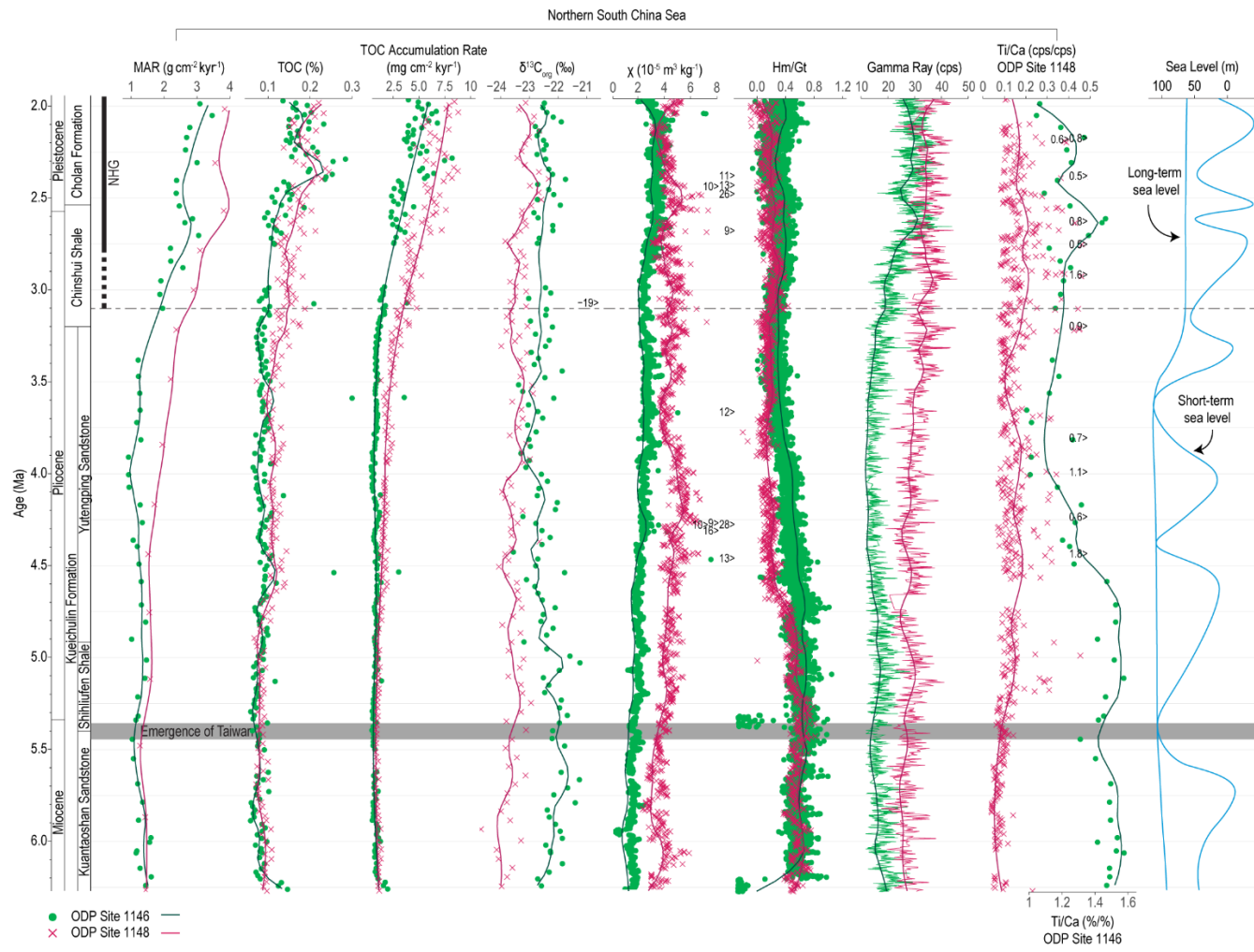
221

222 **Figure 3: Compilation of total organic carbon (TOC), C/N, $\delta^{13}\text{C}_{\text{org}}$, and gamma ray data for the Taiwan Western Foreland Basin**
223 (TWFB), including the Kueichulin Formation (Dashtgard et al., 2021; Hsieh et al., 2023b; Hsieh et al., 2023a), the Chinshui Shale
224 (this study and gamma-ray from Vaucher et al. (2023b)), and the Cholan Formation (this study and gamma-ray from Vaucher et
225 al. (2023b)). Sea-level curves are from Haq and Ogg (2024). “>” indicates data that plot outside of the diagram. The solid lines
226 represent curves fitted using locally estimated scatterplot smoothing (LOESS). TOC, C/N, and $\delta^{13}\text{C}_{\text{org}}$ trends reflect organic
227 carbon sources, and show that marine organic matter content is high in the Kuantaoshan Sandstone, Shihliufen Shale, and
228 Chinshui Shale, contrasting with increased terrestrial input in the Yutengping Sandstone and Cholan Formation. Gamma-ray
229 data indicate lithological variability, and correlate with sea-level changes.

230 At ODP Site 1146 (Figure 4), MAR ($n=59$) and TOC ($n = 225$) values remain relatively stable until ~ 3.3 Ma (averaging 1.2
231 $\pm 0.2 \text{ g cm}^{-2} \text{ kyr}^{-1}$ and $0.08 \pm 0.03\%$, respectively), after which both increase, with a maximum MAR of $3.5 \text{ cm}^{-2} \text{ kyr}^{-1}$, and
232 maximum TOC of 0.3% , accompanied by greater TOC variability. This is reflected in the TOC accumulation rate ($n = 225$),

233 which shows increasing trends also since \sim 3.3 Ma, from an average of $9.6 \pm 3.7 \times 10^{-4}$ to $3.7 \pm 1.8 \times 10^{-3}$ mg cm $^{-2}$ kyr $^{-1}$.
234 $\delta^{13}\text{C}_{\text{org}}$ (n = 113) show a gradual decrease from \sim 5.7–4 Ma from an average of -21.8 ± 0.4 to $-22.2 \pm 0.6\text{\textperthousand}$, then stabilises.
235 Magnetic susceptibility (n = 2747) increases through the record from an average of $\sim 1.6 \pm 0.4$ to $2.5 \pm 1 \times 10^{-5}$ m 3 kg $^{-1}$ from
236 5–3 Ma, with accelerated increase after \sim 3 Ma. Hm/Gt ratios (n = 8196) decrease gradually from \sim 4.75–3 Ma (from an
237 average of 0.56 ± 0.3 to 0.35 ± 0.1 , before showing greater amplitude variability. Gamma-ray values (n = 2551) remain
238 relatively stable (16.2 ± 3.3 API) until \sim 3.2 Ma with when both values and amplitudes rise (26.7 ± 5.7 API). The Ti/Ca
239 record (%%, n = 53) shows an overall decreasing trend from \sim 4.6 Ma–3.5 Ma from an average of 1.5 ± 0.07 to 1.2 ± 0.1 .
240 At ODP Site 1148 (Figure 4), MAR values (n = 15) remain stable with a slight increase at \sim 5.5 Ma from an average of $1.4 \pm$
241 0.009 to 1.6 ± 0.2 g cm $^{-2}$ kyr $^{-1}$, followed by a sharper increase near \sim 3.5 Ma to a maximum of 3.5 g cm $^{-2}$ kyr $^{-1}$. TOC values (n
242 = 220), as well as TOC accumulation rates (n = 220), are stable from \sim 6.27–4.7 Ma (averaging $0.08 \pm 0.01\%$ and $1.1 \pm 0.2 \times$
243 10^{-3} mg cm $^{-2}$ kyr $^{-1}$, respectively. Both TOC and TOC accumulation rates increase from \sim 4.7–4.5 Ma to $0.11 \pm 0.01\%$ and 1.9
244 $\pm 0.3 \times 10^{-3}$ mg cm $^{-2}$ kyr $^{-1}$, then stabilize until \sim 3.5 Ma, and then increased again (exceeding 0.2% and 5×10^{-3} mg cm $^{-2}$ kyr $^{-1}$,
245 respectively) with greater amplitude. MAR, TOC, and TOC accumulation rates also exceed values measured from Site 1146
246 since \sim 4.7 Ma by 20–60%. $\delta^{13}\text{C}_{\text{org}}$ (n = 110) is broadly stable, increasing near \sim 2.75 Ma from an average of -23.2 ± 0.3 to $-$
247 $22.8 \pm 0.4\text{\textperthousand}$. Magnetic susceptibility values (n = 1249) show a gradual increase from \sim 5.4–4.3 Ma from an average of $3.6 \pm$
248 0.6 to $4.9 \pm 0.8 \times 10^{-5}$ m 3 kg $^{-1}$, then a decrease until \sim 3.5 Ma to an average of $4.6 \pm 1.2 \times 10^{-5}$ m 3 kg $^{-1}$. The values remain low
249 after \sim 3.5 Ma, with amplitudes deceasing after \sim 2.75 Ma. Hm/Gt (n = 1678) declines from \sim 5.4–4.6 Ma from an average of
250 0.61 ± 0.08 to 0.2 ± 0.06 , then stabilizes and slightly increases from \sim 3.2–2.9 Ma. Gamma-ray values (n = 1249) are high
251 from \sim 5.4–4.9 Ma, averaging 29.5 ± 3.8 API, then decrease and stabilize before rising again after \sim 3.5 Ma to an average of
252 35 ± 4.2 API. The Ti/Ca ratios (cps/cps, n = 646) increase overall from \sim 5.4 Ma, from an average of 0.07 ± 0.03 to $0.16 \pm$
253 0.1 , with increasing amplitude variability.

254



255
256 **Figure 4: Compilation of sediment core data from ODP Sites 1146 and 1148 in the northern South China Sea, including mass**
257 **accumulation rate (MAR; Wan et al., 2010a; Wang et al., 2000a), TOC and $\delta^{13}\text{C}_{\text{org}}$ (this study), mass-specific magnetic**
258 **susceptibility (χ ; Wang et al., 2005a; Wang et al., 2000a), hematite/goethite (Hm/Gt; Wang et al., 2000b; Clift, 2006), gamma ray**
259 **(Wang et al., 2000b, a), and Ti/Ca (Wan et al., 2010a; Hoang et al., 2010). Sea-level curves are from Haq and Ogg (2024). “>”**
260 **indicates data that plot outside of the diagram. The solid lines represent curves fitted using locally estimated scatterplot smoothing**
261 **(LOESS). The figure illustrates the contrasting sedimentary and geochemical responses between the two ODP sites, driven by**
262 **tectonic uplift, climate variability, and changes in ocean circulation.**

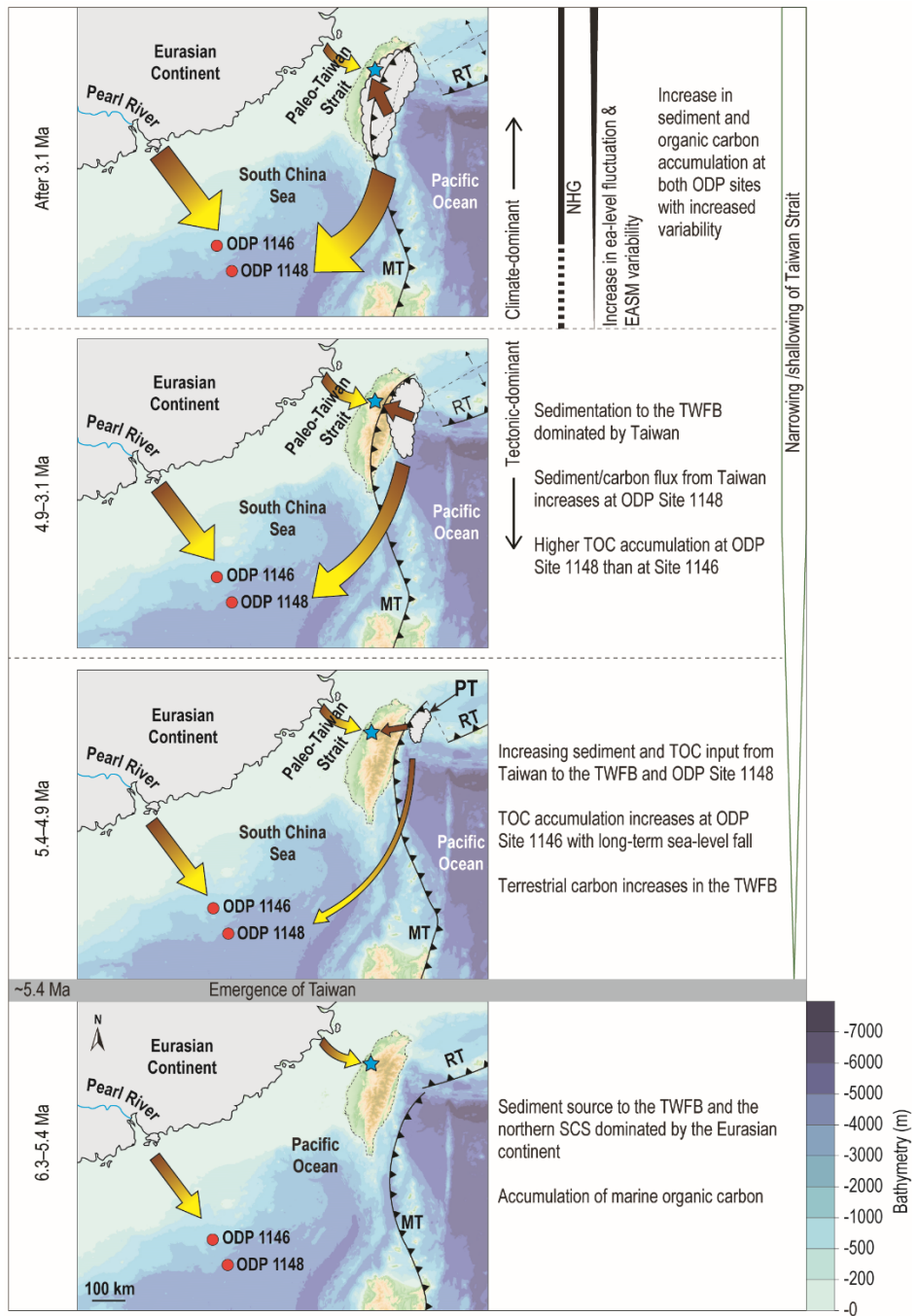
263 **5 Discussion**

264 **5.1 Spatial variability in sediment provenance and distribution in the northern South China Sea**

265 Provenance exerts a first-order control on sedimentary records in the SCS, owing to the region’s complex geology and active
266 tectonism, which channels sediment contributions from multiple major rivers (e.g., Clift et al., 2014; Clift et al., 2022; Horng
267 and Huh, 2011; Kissel et al., 2016, 2017; Liu et al., 2009c; Liu et al., 2007; Liu et al., 2010b; Liu et al., 2016; Wan et al.,

268 2010c; Milliman and Syvitski, 1992). During most of the Neogene, the Pearl River supplied the dominant sediment flux to
269 the northern SCS (Clift et al., 2002; Li et al., 2003). The emergence of the Taiwan orogen in the early Pliocene
270 fundamentally reorganised this system: by ~5.4 Ma, and especially after ~4.9 Ma, Taiwan had become a major sediment
271 source to the adjacent TWFB and the wider SCS, as a result of rapid uplift and intense erosion and south-westward collision-
272 zone migration (Figure 5; Liu et al., 2010b; Hsieh et al., 2023b; Hu et al., 2022). This change in sediment provenance is
273 tectonically driven and underscores the need to disentangle tectonic from climatic signals in SCS sedimentary archives (Clift
274 et al., 2014; Hsieh et al., 2024).

275 This diversity in sediment sources and mixing is reflected at ODP Sites 1146 and 1148, where the sediment records differ
276 despite their spatial proximity. MAR, magnetic susceptibility, Hm/Gt and gamma-ray records diverge between the two sites
277 until ~3 Ma (Figure 4). At ODP Site 1146, located on the continental slope, sediments are primarily derived from Eurasia
278 (Figure 5). At Site 1146, major element and clay mineral compositions point to a mixture of sources dominated by the Pearl
279 River, with additional inputs from the Yangtze River, Taiwan, Luzon, and loess (Wan et al., 2007a; Liu et al., 2003; Hu et
280 al., 2022). Pearl River sediment deposition is controlled by long-term sea-level changes and East Asian Monsoon variability
281 (e.g., Liu et al., 2016; Clift, 2006), but its delivery to the open basin is strongly constrained by alongshore and surface- to
282 intermediate-water currents that funnel most material along the continental shelf and slope (Liu et al., 2010b; Liu et al., 2016;
283 Wan et al., 2007a; Liu et al., 2009a).



285 **Figure 5:** Summary of different controls on sediment and carbon accumulation over time in the Taiwan Western Foreland Basin
 286 (blue star) and the ODP sites (orange circles) in the northern South China Sea. The size of the arrows indicates relative
 287 proportions of sediment flux, and brown indicates accumulation of terrestrial organic carbon, while yellow indicates marine
 288 organic carbon. The abbreviations MT = Manilla Trench, RT = Ryukyu Trench, and PT = proto-Taiwan. These differences in
 289 organic carbon source (i.e., terrestrial vs. marine) and carbon accumulation highlight the spatial heterogeneity in sedimentary and

290 geochemical records within the northern South China Sea, shaped by the interplay of tectonic and climatic processes. Bathymetric
291 map from Gebco Compilation Group, 2025).

292 In contrast, ODP Site 1148, located on the continental rise, records a stronger Taiwanese imprint (i.e., less contribution from
293 Eurasia; Figure 5). Prior to ~6.5 Ma, major element data suggest a mixture of Pearl River and Taiwan inputs, but since the
294 onset of Taiwan orogenesis (~6.5 Ma), Taiwanese material has increasingly dominated (Hu et al., 2022). Isotopic ($^{87}\text{Sr}/^{86}\text{Sr}$,
295 ε_{Nd}) records, and clay mineralogy showing increasing illite with corresponding decreasing kaolinite near ~5 Ma corroborate
296 Taiwan as the dominant sediment contributor to the northern SCS since its emergence after ~5.4 Ma (Bertaz et al., 2024;
297 Boulay et al., 2005; Clift et al., 2014; Hsieh et al., 2023b). Erosion of modern and ancient Taiwan is primarily driven by
298 tropical-cyclone precipitation (Dashtgard et al., 2021; Vaucher et al., 2021; Galewsky et al., 2006; Chen et al., 2010; Chien
299 and Kuo, 2011; Janapati et al., 2019). Under warmer Pliocene climates (Fedorov et al., 2010; Yan et al., 2016) such storms
300 were likely more frequent and intense (e.g., Yan et al., 2019), and especially if coinciding with EASM circulation, would
301 have driven exceptionally high precipitation (Chen et al., 2010; Chien and Kuo, 2011; Kao and Milliman, 2008; Lee et al.,
302 2015; Liu et al., 2008) and sediment export (Vaucher et al., 2023b). Sediment derived from Taiwan is subsequently
303 redistributed into the northern SCS by downslope deep currents (Liu et al., 2010b; Liu et al., 2016; Hu et al., 2012; Liu et al.,
304 2013). The emergence of Taiwan also reconfigured regional circulation, establishing a westward Kuroshio branch that
305 delivered additional sediment from Taiwan and the Philippines (i.e., the Luzon Arc) into the northern basin (Liu et al., 2016).
306 The difference in sediment provenance and transport pathways between the continental slope and continental rise is reflected
307 in the contrasting proxy trends observed at both ODP sites (Figure 4). At ODP Site 1146, the long-term increase in magnetic
308 minerals since ~6.27 Ma reflects increased sediment input from Eurasia that is comparatively enriched in magnetic minerals
309 than sediment from Taiwan (Horng and Huh, 2011; Hsieh et al., 2023b). Concurrently, low gamma-ray values and declining
310 Ti/Ca until ~3 Ma also reflect increased delivery of sand-rich, clastic detritus, while the decreasing Hm/Gt suggests a
311 progressive weakening of the EASM rainfall and seasonality. Together, these proxy signals are consistent with global trends
312 of long-term cooling and falling global mean sea level during this interval (Wan et al., 2007b; Haq et al., 1987; Miller et al.,
313 2020; Westerhold et al., 2020; Holbourn et al., 2021; Berends et al., 2021; Rohling et al., 2014; Jakob et al., 2020; Haq and
314 Ogg, 2024), as well as with evidence of diminished chemical weathering and progressive weakening of the EASM system
315 (Clift et al., 2014; Wan et al., 2006; Wan et al., 2010a; Wan et al., 2010b; Clift, 2025; Li et al., 2004; Wang et al., 2019).
316 This interpretation is further supported by declining K/Al ratios observed at ODP Site 1146 between 5 and 3.8 Ma by Tian et
317 al. (2011), which likewise indicate reduced chemical weathering and a shift towards long-term drying, which began ~10 Ma
318 in the region (Clift, 2025; Clift et al., 2014).

319 At ODP Site 1148, MAR increases near the onset of Taiwan's orogenesis (~5.4 Ma), corresponding to enhanced sediment
320 export from rapid erosion of the emerging orogen. An increase in magnetic susceptibility is also observed ~5.4–4.3 Ma
321 (Figure 4), consistent with the erosion of passive-margin seafloor sediments enriched in magnetic minerals that was uplifted
322 during the early stages of Taiwan's orogenesis (Hsieh et al., 2023b). After ~4.3 Ma, magnetic susceptibility declines,
323 coinciding with the deposition of the Yutengping Sandstone and increasing influx of sediment derived from the

324 metasedimentary core of Taiwan, which is comparatively depleted in magnetic minerals (Hsieh et al., 2023b). Unlike Site
325 1146, the Hm/Gt record at Site 1148 does not appear to track long-term monsoon drying. Rather, the abrupt decrease in the
326 Hm/Gt record at ~5.4 Ma is attributed to the influx of hematite-depleted sediment from Taiwan as it emerged from the
327 Pacific Ocean. The dispersal of Taiwan-sourced sediment into the northern SCS was facilitated by deep-water currents and
328 by the westward-flowing Kuroshio Branch, both of which developed following the formation of the Taiwan and Luzon
329 straits during orogenesis. Changes in ocean circulation during the early to middle Pliocene are also captured by K/Al records,
330 which show contrasting trends between intermediate water depths (e.g., Site 1146) and deep water settings (e.g., Site 1148),
331 which is interpreted as reflecting shifts in sediment dispersal pathways to the northern SCS (Tian et al., 2011). The
332 subsequent rise in Hm/Gt near ~3.2 Ma is attributed to the northward remobilization of Taiwan-sourced sediment following
333 the formation of the Taiwan Warm Current (Figure 3; Hsieh et al., 2024). The gamma-ray record also tracks the orogenic
334 evolution of Taiwan at ODP Site 1148 (Figure 4) and parallels observations from the TWFB (Figure 3): values are elevated
335 during the deposition of mudstone-rich Shihliufen Shale, decrease during formation of sand-dominated Yutengping
336 Sandstone and rise again with the deposition of mudstone-rich Chinshui Shale and Cholan Formation. The increase in
337 sediment export from Taiwan is also reflected in the Ti/Ca record, which increases after ~5.4 Ma, in response to intensified
338 physical erosion and elevated terrestrial flux linked to the onset of Taiwan orogenesis.

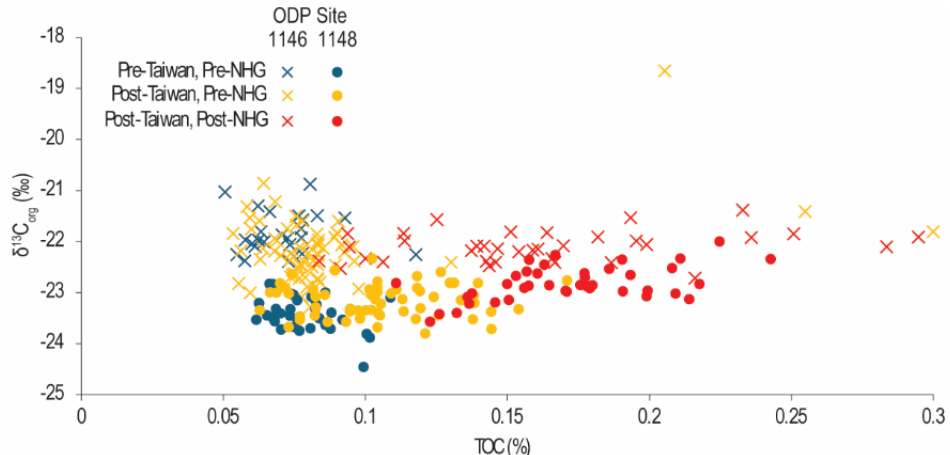
339 After ~3 Ma, the onset of Northern Hemisphere Glaciation (NHG) resulted in enhanced seasonality and an intensification of
340 the EASM (Figure 5; Clift, 2025; Wan et al., 2006; Clift et al., 2014; Wan et al., 2007a; Wan et al., 2007b). Although global
341 cooling characterized the late Plio-Pleistocene (Lisicki and Raymo, 2005), sea-surface temperatures in the northwest Pacific
342 remained sufficiently high (26.5–27.0°C) to sustain tropical cyclone activity (Tory and Frank, 2010). This combined
343 influence of intensified EASM and frequent tropical-cyclone precipitation promoted elevated sediment production and large-
344 scale export of fine-grained material enriched in TOC from river catchments into offshore depocenters. This is reflected in
345 both sites by higher gamma-ray values, increased MAR, and rising Ti/Ca ratios (Figure 4). Enhanced seasonality is further
346 expressed in the greater amplitude observed in gamma-ray, Hm/Gt, and Ti/Ca records.

347 **5.2 Influence of terrestrial sediment export vs. primary production on carbon burial**

348 Organic carbon buried in the SCS can be broadly divided into two components: (1) terrestrial organic matter derived from
349 rock, soil, and terrestrial vegetation exported from adjacent landmasses by precipitation-driven erosion, and (2) marine
350 organic matter produced by primary productivity and exported to the seafloor.

351 At Site 1146, organic carbon accumulation, like bulk sediment accumulation, is primarily controlled by long-term global
352 sea-level fall associated with the onset and intensification of NHG (Figure 5). Total organic carbon values are closely
353 coupled with MAR, with increases in sediment flux consistently accompanied by higher TOC concentrations (Figure 4).
354 Although $\delta^{13}\text{C}_{\text{org}}$ values show a modest decline between ~5.7 and 4.5 Ma, which is consistent with episodic dilution by
355 terrestrial organic inputs, values remain within the marine range (Table 1). The gradual increase in terrestrial organic matter
356 at ODP Site 1146 is interpreted to reflect increased Eurasian clastic influx under conditions of long-term sea-level fall. The

357 cross-plot of $\delta^{13}\text{C}_{\text{org}}$ and TOC also shows no distinct shift between organic matter delivered to Site 1146 before and after the
 358 emergence of Taiwan. As sediment transported eastward from the Eurasian margin would have longer residence times in the
 359 ocean, the dilution of land-derived organic material by marine organic material would increase, resulting in a more marine
 360 $\delta^{13}\text{C}_{\text{org}}$ signature (Dashtgard et al., 2021) which supports the interpretation that organic material is derived mainly from
 361 Eurasia via the Pearl River (Figure 6).



362
 363 **Figure 6: Cross-plot of $\delta^{13}\text{C}_{\text{org}}$ and TOC measured from ODP Sites 1146 and 1148. Values are grouped according to major tectonic**
 364 **and climate changes: 1) pre-emergence of Taiwan and pre-Northern Hemisphere Glaciation, 2) post-emergence of Taiwan and**
 365 **pre-Northern Hemisphere Glaciation, and 3) post-emergence of Taiwan and post-Northern Hemisphere Glaciation. Note the**
 366 **distinct trends before and after Taiwan's emergence and Northern Hemisphere Glaciation. Site 1146 reflects Eurasian sediment**
 367 **input with marine organic matter dominance, while Site 1148 highlights Taiwan's influence, with enhanced marine productivity**
 368 **linked to nutrient export.**

369 In contrast, carbon burial at Site 1148 is primarily linked to the uplift and erosion of Taiwan and associated increase in
 370 sediment and nutrient delivery to the marine environment (Figure 5). The onset of Taiwan's emergence at ~5.4 Ma coincides
 371 with a marked rise in MAR, followed by an increase in TOC beginning near ~4.9 Ma (Figure 4). This pattern reflects
 372 significant export of terrestrial sediment from the rapidly uplifting Taiwan orogen, a process further amplified by the
 373 coupling between tropical cyclone and monsoon precipitation (Vaucher et al., 2023b). Notably, TOC increases
 374 proportionally with MAR, implying that carbon burial was not diluted by high sediment flux but rather enhanced by
 375 intensified sediment export and/or better preserved by rapid burial, highlighting the role of Taiwan as a contributor of
 376 organic carbon in the northern SCS. The influence of sedimentation from Taiwan on organic matter buried at Site 1148 is
 377 also evident from the cross-plot between $\delta^{13}\text{C}_{\text{org}}$ and TOC, which shows a distinct increase in TOC prior to and after the
 378 emergence of Taiwan (Figure 6).

379 Taiwan's steep topography and active tectonics generate exceptionally high sediment yields to adjacent marine systems (Liu
 380 et al., 2013; Dadson et al., 2003; Dadson et al., 2004). Turbidity currents, especially via submarine canyon systems (e.g., the
 381 Gaoping Submarine Canyon in southern Taiwan), efficiently transport organic-rich sediment eroded from Taiwan to deep-
 382 sea environments approximately 260 km offshore into the northeastern Manila Trench (Liu et al., 2009b; Liu et al., 2016;

383 Zheng et al., 2017; Yu et al., 2009; Nagel et al., 2018). Within the TWFB, this process is manifested as an abrupt increase in
384 terrestrial organic matter and sand-rich deposition near ~4.9 Ma with the emplacement of the Yutengping Sandstone (Figure
385 4). At Site 1148, TOC increases markedly in association with the emergence of Taiwan, and $\delta^{13}\text{C}_{\text{org}}$ values remain stable
386 above -25‰. While C_4 plants are characterized by high $\delta^{13}\text{C}_{\text{org}}$ values (Table 1), and an expansion of C_4 plants in the South
387 China region has been documented since 35 Ma (Li et al., 2023; Xue et al., 2024), the organic carbon at Site 1148 are
388 interpreted to be of marine in origin as C_3 plants remain the dominant vegetation type in the study area (Luo et al., 2024; Still
389 et al., 2003; Wang and Ma, 2016). Furthermore, sediment provenance markers (Section 5.1) indicate an influx of Taiwan-
390 sourced material to Site 1148 after the emergence of Taiwan, and $\delta^{13}\text{C}_{\text{org}}$ values in the TWFB reflect an increase in terrestrial
391 organic matter. The presence of Taiwan-sourced material combined with high proportions of marine organic carbon at Site
392 1148 suggests that terrestrial organic matter from Taiwan was largely confined to proximal coastal environments, and that
393 enhanced carbon burial in deeper settings reflects processes beyond direct terrigenous input. Likewise, terrestrial organic
394 matter contribution from the Pearl River into deeper-water depocenters is limited, as sediment is dispersed along the
395 continental shelf by alongshore and shallow- to intermediate-water currents (Liu et al., 2010b; Liu et al., 2016; Wan et al.,
396 2007a). During transport and sedimentation, degradation does not appear to significantly alter the isotopic composition of
397 organic matter, since there is little fractionation between reactants and products. If post-depositional alteration were a
398 dominant control, $\delta^{13}\text{C}_{\text{org}}$ values should become progressively less negative with depth, as lighter isotopes are preferentially
399 removed. However, the $\delta^{13}\text{C}_{\text{org}}$ records from the two sites show distinct trends, suggesting that the influence of post-
400 depositional isotopic fractionation is insignificant.

401 Taiwan's rapid denudation delivers large quantities of sediment and nutrients to the northern SCS, profoundly shaping basin
402 productivity and carbon cycling. The export of bioessential nutrients stimulates intense coastal primary production, as
403 reflected by modern chlorophyll-a and nitrogen distributions that peak along Taiwan's coast before rapidly declining
404 offshore due to swift uptake (Kao et al., 2006; Ge et al., 2020; Huang et al., 2020). Episodic inputs from tropical cyclones,
405 which contribute up to 80% of summer particulate organic carbon, further amplify productivity and promote lateral dispersal
406 of sediments (Liu et al., 2013). Marine organic matter produced through enhanced coastal productivity could be redistributed
407 by deep-water contour currents and mesoscale eddies, (Lüdmann et al., 2005; Zhang et al., 2014; Zhao et al., 2015; Hsieh et
408 al., 2024), enabling its bypass into the deeper water depths and resulting in the marine signature of the $\delta^{13}\text{C}_{\text{org}}$ records from
409 the northern SCS.

410 Fluvial input from Taiwan, especially via submarine canyon systems, makes the northern SCS a depocenter for organic
411 carbon burial, with important implications for the basin's sedimentary architecture, long-term carbon budget, and even
412 hydrocarbon source rock potential (Kao et al., 2006). Paleoceanographic records indicate that productivity and organic
413 carbon burial increased during glacial periods (Thunell et al., 1992), likely driven by nutrient delivery from Taiwan's
414 sediments that enhanced the biological pump and contributed to regional carbon drawdown. In the modern setting, episodic
415 sediment fluxes during typhoons sustain unusually high chlorophyll-a concentrations in deep SCS waters relative to the
416 global ocean (Shih et al., 2019). Moreover, northeast monsoon-driven mixing between the China Coastal Current and

417 Taiwan Strait Current, reinforced by sediment and nutrient inputs dominantly from Taiwan and the Yangtze River, sustains
418 elevated productivity in the northern SCS (Huang et al., 2020). Collectively, these processes highlight Taiwan's sediment
419 flux as a key linkage between monsoon forcing, nutrient cycling, and primary production across both modern and in the past.

420 **5.3 Influence of climate and monsoon on carbon burial**

421 In the TWFB, carbon geochemistry and gamma-ray data largely reflect the evolution of the foreland basin synchronously
422 with the shifts in the regional climate regime (Figure 3). During the deposition of the Chinshui Shale in the late Pliocene
423 (~3.2 to 2.5 Ma), reconstructions for the northwest Pacific show relatively high global sea levels and stable sea-surface
424 temperatures (Li et al., 2011; Berends et al., 2021). Such conditions favoured the accumulation of fine-grained sediment,
425 while elevated sea levels deepened the TWFB and promoted offshore depositional environments-both of which are
426 expressed in the Chinshui Shale (e.g., Nagel et al., 2013; Vaucher et al., 2023b). Greater water depths and increased distance
427 from the terrestrial sediment sources also enhanced the relative contribution of marine organic matter. The gamma-ray record
428 of the TWFB strata further reveals depositional cycles related to interactions between EASM and tropical cyclone
429 precipitation after ~4.92 Ma, with variability expressed at both short-eccentricity and precession frequency bands (Vaucher
430 et al., 2023b; Hsieh et al., 2023a).

431 During the early Pleistocene, with deposition of the Cholan Formation (~2.5–1.95 Ma), global sea level and regional sea-
432 surface temperatures became markedly more variable (Li et al., 2011; Berends et al., 2021). The continued uplift and
433 southwest migration of Taiwan promoted the development of shallow-marine depositional environments recorded in the
434 Cholan Formation (e.g., Pan et al., 2015; Vaucher et al., 2021; Vaucher et al., 2023a; Vaucher et al., 2023b). This is
435 expressed in the gamma-ray and carbon records as an increase in terrestrially sourced, sandstone-rich intervals with high
436 variability (Figure 3). The enhanced export of coarser-grained sediment from land to sea is likely related to the onset of
437 NHG, when repeated sea-level minima promoted clastic delivery to the basin (Vaucher et al., 2021; Vaucher et al., 2023b).
438 In addition, global climate deterioration related to NHG intensified and destabilised the EASM (Wan et al., 2006; Wan et al.,
439 2007a). Paleoclimate reconstructions from East Asia document a strengthening of the EASM during the late Pliocene,
440 generally near ~3.5 Ma (Zhang et al., 2009; Yang et al., 2018; Yan et al., 2018; Xin et al., 2020; Nie et al., 2014; Hoang et
441 al., 2010). While the causal relationship between monsoon intensity and NHG remains debated (Zhang et al., 2009; Xin et
442 al., 2020; Wan et al., 2010b; Nie et al., 2014), long-term global cooling and sea-level fall coupled with monsoon and
443 tropical cyclone precipitation likely acted together to amplify sediment export from land to sea (Vaucher et al., 2023b). In
444 the northern SCS, MAR and TOC values and amplitudes at both ODP sites increased after ~3 Ma, consistent with increased
445 sediment export (Figure 4; Figure 5). At the same time, $\delta^{13}\text{C}_{\text{org}}$ values at ODP Site 1148 increases after ~3 Ma, suggesting
446 increasing marine contribution to organic carbon. This trend is attributed to enhanced marine primary production driven by
447 nutrient enrichment. Independent evidence for increased marine primary productivity in this interval comes from elevated
448 abundances of planktonic foraminifera *Neogloboquadrina dutertrei* and higher biogenic silica production (Wang et al.,
449 2005b).

450 **6 Conclusion**

451 Analyses of late-Miocene to early Pleistocene sedimentary and geochemical records from shallow-marine strata of the
452 Taiwan Western Foreland Basin and deep-sea sediment cores from the northern South China Sea (SCS) provide clear
453 evidence for shifting pathways of carbon erosion, transport, and burial shaped by the interplay between tectonic forcing,
454 climate variability, and oceanographic processes.

455 Sediment provenance reveals marked spatial heterogeneity between the continental slope (ODP Site 1146) and the
456 continental rise (ODP Site 1148), highlighting the influence of tectonic uplift and evolving ocean circulation on sediment
457 mixing and deposition. Prior to ~5.4 Ma, sediment delivery to the northern SCS was dominated by Pearl River discharge.
458 Taiwan's rapid emergence and erosion at ~5.4 Ma supplied large volumes of clastic material to the basin, which is expressed
459 in sediment provenance records at Site 1148, whereas Site 1146 remained strongly influenced by Eurasian sources. Pearl
460 River sediments were dispersed along the continental shelf and slope by alongshore and shallow- to intermediate-water
461 currents but were largely obstructed from reaching deeper water depths by the northward-flowing Kuroshio Current and the
462 shallow Taiwan Strait.

463 The onset of Northern Hemisphere Glaciation (NHG; ~3 Ma) further amplified sediment erosion and export across the basin.
464 Long-term global cooling and sea-level fall, coupled with enhanced seasonality, drove the intensification of the East Asian
465 Summer Monsoon. The resulting increase in monsoon rainfall, as well as persistent tropical cyclone activity, drove
466 synchronous increases in mass-accumulation rate (MAR), magnetic susceptibility, and Ti/Ca values at both ODP sites,
467 demonstrating the strong climatic imprint on sediment export. In addition, slightly higher $\delta^{13}\text{C}_{\text{org}}$ values after ~3 Ma indicate
468 a greater marine contribution to organic matter, attributed to enhanced nutrient-driven marine primary production.

469 Organic carbon burial likewise reflects the combined influence of tectonic and climate forcing. At ODP Site 1146, total
470 organic carbon (TOC) accumulation parallels MAR and is primarily controlled by long-term sea-level fall and NHG
471 intensification. $\delta^{13}\text{C}_{\text{org}}$ values indicate that the bulk of organic matter remained marine in origin, with minor terrestrial
472 contribution linked to Eurasian sediment export rather than to Taiwan's orogenesis. At ODP Site 1148, by contrast, organic
473 carbon burial is closely tied to the Taiwan's uplift and erosion. Importantly, TOC scales proportionally with MAR, implying
474 that organic matter burial was enhanced—not diluted—by high sediment flux. Despite Taiwan's steep relief, rapid tectonic
475 uplift, and frequent typhoon- and monsoon-driven erosion generating exceptional sediment yields, $\delta^{13}\text{C}_{\text{org}}$ values indicate
476 that most buried organic carbon was marine. This suggests that Taiwan's erosion enhanced nutrient supply, stimulating
477 coastal primary productivity. Marine organic matter produced in these settings was then redistributed offshore by turbidity
478 currents through submarine canyon systems, bypassing the shelf and slope and accumulating in deep-sea depocenters of the
479 northern SCS.

480 Overall, this study highlights the importance of resolving spatial heterogeneities in sedimentary climate archives.
481 Disentangling the competing influences of tectonics and climate on sediment supply and carbon burial is critical for robust
482 intercomparison of paleoclimate records, and for reconciling apparent inconsistencies among proxy reconstructions. Our

483 findings also demonstrate that terrestrial sediment export contributes to carbon drawdown via two distinct pathways: (1)
484 direct burial of eroded terrestrial organic matter and (2) nutrient supply that fuels marine primary production and subsequent
485 burial of marine organic matter. This work establishes a direct link between the tectonic evolution of an arc-continent
486 collisional orogen and changes in carbon storage in adjacent basins, and disentangles the mechanisms by which the erosion
487 of mid-latitude orogens contributed to long-term carbon sequestration.

488 **Acknowledgements**

489 We would like to thank Dr. Yusuke Kubo at the Japan Agency for Marine-Earth Science and Technology for access to the
490 ODP Site 1146 and 1148 core samples. This research was supported financially through the Institute of Earth Sciences
491 Postdoctoral fellowship awarded to A.I. Hsieh from the University of Lausanne. R. Vaucher acknowledges the Swiss
492 National Science Foundation Postdoc.Mobility Grant (P400P2_183946) which supported him during data collection from the
493 Cholan Formation. We express our gratitude to Kuo-Hang Chen for supporting the magnetostratigraphic analysis, Tiffany
494 Monnier for assisting in sample processing and analysis, and Ling-Wen Liu for elemental and isotope analyses. We are
495 grateful for the constructive feedback from an anonymous referee and Prof. Shannon Dulin, as well as the support from the
496 editor, Prof. Lynn Soreghan, who helped to greatly improve this manuscript.

497 **Conflict of interest**

498 The authors declare no conflict of interest

499 **Author contributions**

500 A.I.H. was responsible for the design and conceptualization of this study, supervised by S.J. Data collection was completed
501 by A.I.H., S.B., and R.V. A.I.H., T.A., L.L., B.B., L.K., and P.-L.W. were responsible for sample analysis. T.A., L.L., S.B.,
502 R.V., and S.J provided support in the interpretation of sedimentary paleoenvironmental proxies. All co-authors reviewed and
503 approved the manuscript.

504 **Data availability**

505 The data that support the findings of this study can be found on PANGAEA.

506 **References**

507 Aumont, O., Orr, J. C., Monfray, P., Ludwig, W., Amiotte-Suchet, P., and Probst, J.-L.: Riverine-driven interhemispheric
508 transport of carbon, *Global Biogeochem. Cycles*, 15, 393-405, 10.1029/1999GB001238, 2001.

509 Bayon, G., Patriat, M., Godderis, Y., Trinquier, A., De Deckker, P., Kulhanek, D. K., Holbourn, A., and Rosenthal, Y.:
510 Accelerated mafic weathering in Southeast Asia linked to late Neogene cooling, *Sci. Adv.*, 9, eadf3141,
511 doi:10.1126/sciadv.adf3141, 2023.

512 Behar, F., Beaumont, V., and De B. Penteado, H. L.: Rock-Eval 6 Technology: Performances and Developments, *Oil & Gas*
513 *Science and Technology - Rev. IFP*, 56, 111-134, 10.2516/ogst:2001013, 2001.

514 Berends, C. J., de Boer, B., and van de Wal, R. S. W.: Reconstructing the evolution of ice sheets, sea level, and atmospheric
515 CO₂ during the past 3.6 million years, *Clim. Past*, 17, 361-377, 10.5194/cp-17-361-2021, 2021.

516 Berner, R. A.: The long-term carbon cycle, fossil fuels and atmospheric composition, *Nature*, 426, 323-326,
517 10.1038/nature02131, 2003.

518 Bertaz, J., Liu, Z., Colin, C., Dapoigny, A., Lin, A. T.-S., Li, Y., and Jian, Z.: Climatic and Environmental Impacts on the
519 Sedimentation of the SW Taiwan Margin Since the Last Deglaciation: Geochemical and Mineralogical Investigations,
520 *Paleoceanogr. Paleoclimatol.*, 39, e2023PA004745, 10.1029/2023PA004745, 2024.

521 Beusen, A. H. W., Bouwman, A. F., Van Beek, L. P. H., Mogollón, J. M., and Middelburg, J. J.: Global riverine N and P
522 transport to ocean increased during the 20th century despite increased retention along the aquatic continuum,
523 *Biogeosciences*, 13, 2441-2451, 10.5194/bg-13-2441-2016, 2016.

524 Boulay, S., Colin, C., Trentesaux, A., Frank, N., and Liu, Z.: Sediment sources and East Asian monsoon intensity over the
525 last 450 ky. Mineralogical and geochemical investigations on South China Sea sediments, *Palaeogeogr. Palaeoclimatol.*
526 *Palaeoecol.*, 228, 260-277, 10.1016/j.palaeo.2005.06.005, 2005.

527 Burke, K. D., Williams, J. W., Chandler, M. A., Haywood, A. M., Lunt, D. J., and Otto-Bliesner, B. L.: Pliocene and Eocene
528 provide best analogs for near-future climates, *Proc. Nat. Acad. Sci.*, 115, 13288-13293, 10.1073/pnas.1809600115, 2018.

529 Canadell, J. G., Monteiro, P. M. S., Costa, M. H., Cotrim da Cunha, L., Cox, P. M., Eliseev, A. V., Henson, S., Ishii, M.,
530 Jaccard, S., Koven, C., Lohila, A., Patra, P. K., Piao, S., Rogelj, J., Syampungani, S., Zaehle, S., and Zickfeld, K.: Global
531 Carbon and Other Biogeochemical Cycles and Feedbacks, in: *Climate Change 2021: The Physical Science Basis.*
532 Contribution of Working Group I to the Sixth Assessment Report of the Intergovernmental Panel on Climate Change, edited
533 by: Masson-Delmotte, V., Zhai, P., Pirani, A., Connors, S. L., Péan, C., Berger, S., Caud, N., Chen, Y., Goldfarb, L., Gomis,
534 M. I., Huang, M., Leitzell, K., Lonnoy, E., Matthews, J. B. R., Maycock, T. K., Waterfield, T., Yelekçi, O., Yu, R., and
535 Zhou, B., Cambridge University Press, Cambridge, United Kingdom and New York, NY, USA, 673-816,
536 10.1017/9781009157896.007, 2021.

537 Castelltort, S., Nagel, S., Mouthereau, F., Lin, A. T.-S., Wetzel, A., Kaus, B., Willett, S., Chiang, S.-P., and Chiu, W.-Y.:
538 Sedimentology of early Pliocene sandstones in the south-western Taiwan foreland: Implications for basin physiography in
539 the early stages of collision, *J. Asian Earth Sci.*, 40, 52-71, 10.1016/j.jseas.2010.09.005, 2011.

540 Caves, J. K., Jost, A. B., Lau, K. V., and Maher, K.: Cenozoic carbon cycle imbalances and a variable weathering feedback,
541 *Earth Planet. Sci. Lett.*, 450, 152-163, 10.1016/j.epsl.2016.06.035, 2016.

542 Chen, C.-W., Oguchi, T., Hayakawa, Y. S., Saito, H., Chen, H., Lin, G.-W., Wei, L.-W., and Chao, Y.-C.: Sediment yield
543 during typhoon events in relation to landslides, rainfall, and catchment areas in Taiwan, *Geomorphology*, 303, 540-548,
544 10.1016/j.geomorph.2017.11.007, 2018.

545 Chen, J.-M., Li, T., and Shih, C.-F.: Tropical cyclone- and monsoon-induced rainfall variability in Taiwan, *J. Clim.*, 23,
546 4107-4120, 10.1175/2010jcli3355.1, 2010.

547 Chen, W.-S.: An Introduction to the Geology of Taiwan, Geologic Society of Taiwan, Taipei, Taiwan2016.

548 Cheng, X., Zhao, Q., Wang, J., Jian, Z., Xia, P., Huang, B., Fang, D., Xu, J., Zhou, Z., and Wang, P.: Data Report: Stable
549 Isotopes from Sites 1147 and 1148, 10.2973/odp.proc.sr.184.223.2004, 2004.

550 Chien, F.-C. and Kuo, H.-C.: On the extreme rainfall of Typhoon Morakot (2009), *J. Geophys. Res.*, 116, D05104,
551 10.1029/2010jd015092, 2011.

552 Chmura, G. L. and Aharon, P.: Stable carbon isotope signatures of sedimentary carbon in coastal wetlands as indicators of
553 salinity regime, *J. Coast. Res.*, 11, 124-135, 1995.

554 Cleveland, W. S., Grosse, E., and Shyu, W. M.: Local Regression Models, 1st, Statistical Models in S, Routledge, New
555 York, 10.1201/9780203738535, 1992.

556 Clift, P. D.: Controls on the erosion of Cenozoic Asia and the flux of clastic sediment to the ocean, *Earth Planet. Sci. Lett.*,
557 241, 571-580, 10.1016/j.epsl.2005.11.028, 2006.

558 Clift, P. D.: Variations in aridity across the Asia–Australia region during the Neogene and their impact on vegetation, *Geol.
559 Soc. Lond. Spec. Pub.*, 549, 157-178, 10.1144/SP549-2023-58, 2025.

560 Clift, P. D. and Jonell, T. N.: Himalayan-Tibetan Erosion Is Not the Cause of Neogene Global Cooling, *Geophys. Res. Lett.*,
561 48, e2020GL087742, 10.1029/2020GL087742, 2021.

562 Clift, P. D., Wan, S., and Blusztajn, J.: Reconstructing chemical weathering, physical erosion and monsoon intensity since
563 25Ma in the northern South China Sea: A review of competing proxies, *Earth Sci. Rev.*, 130, 86-102,
564 10.1016/j.earscirev.2014.01.002, 2014.

565 Clift, P. D., Jonell, T. N., Du, Y., and Bornholdt, T.: The impact of Himalayan-Tibetan erosion on silicate weathering and
566 organic carbon burial, *Chem. Geol.*, 656, 122106, 10.1016/j.chemgeo.2024.122106, 2024a.

567 Clift, P. D., Lee, J. I., Clark, M. K., and Blusztajn, J.: Erosional response of South China to arc rifting and monsoonal
568 strengthening; a record from the South China Sea, *Mar. Geol.*, 184, 207-226, 10.1016/S0025-3227(01)00301-2, 2002.

569 Clift, P. D., Du, Y., Mohtadi, M., Pahnke, K., Sutorius, M., and Böning, P.: The erosional and weathering response to arc–
570 continent collision in New Guinea, *J. Geol. Soc.*, 181, jgs2023-2207, 10.1144/jgs2023-207, 2024b.

571 Clift, P. D., Betzler, C., Clemens, S. C., Christensen, B., Eberli, G. P., France-Lanord, C., Gallagher, S., Holbourn, A.,
572 Kuhnt, W., Murray, R. W., Rosenthal, Y., Tada, R., and Wan, S.: A synthesis of monsoon exploration in the Asian marginal
573 seas, *Scientific Drilling*, 31, 1-29, 10.5194/sd-31-1-2022, 2022.

574 Covey, M.: The evolution of foreland basins to steady state: Evidence from the western Taiwan foreland basin, in: *Foreland*
575 *Basins*, edited by: Allen, P. A., and Homewood, P., Blackwell Publishing Ltd., 77-90, 10.1002/9781444303810.ch4, 1986.

576 Dadson, S. J., Hovius, N., Chen, H., Dade, W. B., Lin, J.-C., Hsu, M.-L., Lin, C.-W., Horng, M.-J., Chen, T.-C., Milliman,
577 J., and Stark, C. P.: Earthquake-triggered increase in sediment delivery from an active mountain belt, *Geology*, 32,
578 10.1130/g20639.1, 2004.

579 Dadson, S. J., Hovius, N., Chen, H., Dade, W. B., Hsieh, M.-L., Willett, S. D., Hu, J.-C., Horng, M.-J., Chen, M.-C., Stark,
580 C. P., Lague, D., and Lin, J.-C.: Links between erosion, runoff variability and seismicity in the Taiwan orogen, *Nature*, 426,
581 648-651, 10.1038/nature02150, 2003.

582 Dagg, M., Benner, R., Lohrenz, S., and Lawrence, D.: Transformation of dissolved and particulate materials on continental
583 shelves influenced by large rivers: plume processes, *Cont. Shelf Res.*, 24, 833-858, 10.1016/j.csr.2004.02.003, 2004.

584 Dashtgard, S. E., Löwemark, L., Wang, P.-L., Setiaji, R. A., and Vaucher, R.: Geochemical evidence of tropical cyclone
585 controls on shallow-marine sedimentation (Pliocene, Taiwan), *Geology*, 49, 566-570, 10.1130/g48586.1, 2021.

586 Dowsett, H. J.: The PRISM palaeoclimate reconstruction and Pliocene sea-surface temperature, in: *Deep-Time Perspectives*
587 on Climate Change: Marrying the Signal from Computer Models and Biological Proxies

588 edited by: Williams, M., Haywood, A. M., Gregory, F. J., and Schmidt, D. N., Geological Society of London, 0, 10.1144/tms002.21, 2007.

589 Dürr, H. H., Meybeck, M., Hartmann, J., Laruelle, G. G., and Roubeix, V.: Global spatial distribution of natural riverine
590 silica inputs to the coastal zone, *Biogeosciences*, 8, 597-620, 10.5194/bg-8-597-2011, 2011.

591 Espitalie, J., Deroo, G., and Marquis, F.: La pyrolyse Rock-Eval et ses applications. Première partie, *Rev. Inst. Fr. Pét.*, 40,
592 563-579, 10.2516/ogst:1985035, 1985.

593 Fedorov, A. V., Brierley, C. M., and Emanuel, K.: Tropical cyclones and permanent El Niño in the early Pliocene epoch,
594 *Nature*, 463, 1066-1070, 10.1038/nature08831, 2010.

595 Fedorov, A. V., Brierley, C. M., Lawrence, K. T., Liu, Z., Dekens, P. S., and Ravelo, A. C.: Patterns and mechanisms of
596 early Pliocene warmth, *Nature*, 496, 43-49, 10.1038/nature12003, 2013.

597 Froelich, P. N.: Kinetic control of dissolved phosphate in natural rivers and estuaries: A primer on the phosphate buffer
598 mechanism, *Limnol. Oceanogr.*, 33, 649-668, 10.4319/lo.1988.33.4part2.0649, 1988.

599 Galewsky, J., Stark, C. P., Dadson, S., Wu, C. C., Sobel, A. H., and Horng, M. J.: Tropical cyclone triggering of sediment
600 discharge in Taiwan, *J. Geophys. Res.*, 111, F03014, 10.1029/2005JF000428, 2006.

601 Galy, V., France-Lanord, C., Beyssac, O., Faure, P., Kudrass, H., and Palhol, F.: Efficient organic carbon burial in the
602 Bengal fan sustained by the Himalayan erosional system, *Nature*, 450, 407-410, 10.1038/nature06273, 2007.

603 Ge, J., Torres, R., Chen, C., Liu, J., Xu, Y., Bellerby, R., Shen, F., Bruggeman, J., and Ding, P.: Influence of suspended
604 sediment front on nutrients and phytoplankton dynamics off the Changjiang Estuary: A FVCOM-ERSEM coupled model
605 experiment, *J. Mar. Syst.*, 204, 103292, 10.1016/j.jmarsys.2019.103292, 2020.

606 GEBCO Compilation Group: GEBCO 2025 Grid, 10.5285/37c52e96-24ea-67ce-e063-7086abc05f29, 2025.

607 Green, W. G. and Fearon, R. E.: Well logging by radioactivity, *Geophysics*, 5, 272-283, 1940.

608 Haq, B. U. and Ogg, J. G.: Retraversing the Highs and Lows of Cenozoic Sea Levels, *GSA Today*, 34, 4-11,
609 10.1130/GSATGG593A.1, 2024.

610 Haq, B. U., Hardenbol, J., and Vail, P. R.: Chronology of Fluctuating Sea Levels Since the Triassic, *Science*, 235, 1156-
611 1167, 10.1126/science.235.4793.1156, 1987.

612 Hilton, R. G. and West, A. J.: Mountains, erosion and the carbon cycle, *Nat. Rev. Earth Environ.*, 1, 284-299,
613 10.1038/s43017-020-0058-6, 2020.

614 Hilton, R. G., Galy, A., Hovius, N., Horng, M.-J., and Chen, H.: The isotopic composition of particulate organic carbon in
615 mountain rivers of Taiwan, *Geochim. Cosmochim. Acta*, 74, 3164-3181, 10.1016/j.gca.2010.03.004, 2010.

616 Hilton, R. G., Galy, A., Hovius, N., Horng, M.-J., and Chen, H.: Efficient transport of fossil organic carbon to the ocean by
617 steep mountain rivers: An orogenic carbon sequestration mechanism, *Geology*, 39, 71-74, 10.1130/g31352.1, 2011.

618 Hoang, L. V., Clift, P. D., Schwab, A. M., Huuse, M., Nguyen, D. A., and Zhen, S.: Large-scale erosional response of SE
619 Asia to monsoon evolution reconstructed from sedimentary records of the Song Hong-Yinggehai and Qiongdongnan basins,
620 South China Sea, *Geol. Soc. Lond. Spec. Pub.*, 342, 219-244, doi:10.1144/SP342.13, 2010.

621 Holbourn, A., Kuhnt, W., Clemens, S. C., and Heslop, D.: A ~12 Myr Miocene record of East Asian Monsoon variability
622 from the South China Sea, *Paleoceanogr. Paleoclimatol.*, 36, 10.1029/2021pa004267, 2021.

623 Holbourn, A., Kuhnt, W., Schulz, M., and Erlenkeuser, H.: Impacts of orbital forcing and atmospheric carbon dioxide on
624 Miocene ice-sheet expansion, *Nature*, 438, 483-487, 10.1038/nature04123, 2005.

625 Holbourn, A., Kuhnt, W., Schulz, M., Flores, J.-A., and Andersen, N.: Orbitally-paced climate evolution during the middle
626 Miocene “Monterey” carbon-isotope excursion, *Earth Planet. Sci. Lett.*, 261, 534-550, 10.1016/j.epsl.2007.07.026, 2007.

627 Horng, C.-S.: Age of the Tananwan Formation in Northern Taiwan: A reexamination of the magnetostratigraphy and
628 calcareous nannofossil biostratigraphy, *Terr. Atmos. Ocean Sci.*, 25, 10.3319/tao.2013.11.05.01(tt), 2014.

629 Horng, C.-S. and Huh, C.-A.: Magnetic properties as tracers for source-to-sink dispersal of sediments: A case study in the
630 Taiwan Strait, *Earth Planet. Sci. Lett.*, 10.1016/j.epsl.2011.07.002, 2011.

631 Hoshiba, Y. and Yamanaka, Y.: Along-coast shifts of plankton blooms driven by riverine inputs of nutrients and fresh water
632 onto the coastal shelf: a model simulation, *J. Oceanogr.*, 69, 753-767, 10.1007/s10872-013-0206-4, 2013.

633 Houghton, R. A.: Why are estimates of the terrestrial carbon balance so different?, *Glob. Change Biol.*, 9, 500-509,
634 10.1046/j.1365-2486.2003.00620.x, 2003.

635 Hsieh, A. I., Dashtgard, S. E., Clift, P. D., Lo, L., Vaucher, R., and Löwemark, L.: Competing influence of the Taiwan
636 orogen and East Asian Summer Monsoon on South China Sea paleoenvironmental proxy records, *Palaeogeogr.*
637 *Palaeoclimatol. Palaeoecol.*, 635, 111933, 10.1016/j.palaeo.2023.111933, 2024.

638 Hsieh, A. I., Vaucher, R., Löwemark, L., Dashtgard, S. E., Horng, C. S., Lin, A. T.-S., and Zeeden, C.: Influence of a rapidly
639 uplifting orogen on the preservation of climate oscillations, *Paleoceanogr. Paleoclimatol.*, 38, e2022PA004586,
640 10.1029/2022PA004586, 2023a.

641 Hsieh, A. I., Dashtgard, S. E., Wang, P. L., Horng, C. S., Su, C. C., Lin, A. T., Vaucher, R., and Löwemark, L.: Multi-proxy
642 evidence for rapidly shifting sediment sources to the Taiwan Western Foreland Basin at the Miocene–Pliocene transition,
643 *Basin Res.*, 35, 932-948, 10.1111/bre.12741, 2023b.

644 Hsieh, A. I., Vaucher, R., MacEachern, J. A., Zeeden, C., Huang, C., Lin, A. T., Löwemark, L., and Dashtgard, S. E.:
645 Resolving alloigenic forcings on shallow-marine sedimentary archives of the Taiwan Western Foreland Basin,
646 *Sedimentology*, 72, 1755-1785, 10.1111/sed.70020, 2025.

647 Hu, D., Böning, P., Köhler, C. M., Hillier, S., Pressling, N., Wan, S., Brumsack, H. J., and Clift, P. D.: Deep sea records of
648 the continental weathering and erosion response to East Asian monsoon intensification since 14 ka in the South China Sea,
649 *Chem. Geol.*, 326-327, 1-18, 10.1016/j.chemgeo.2012.07.024, 2012.

650 Hu, J., Kawamura, H., Li, C., Hong, H., and Jiang, Y.: Review on current and seawater volume transport through the Taiwan
651 Strait, *J. Oceanogr.*, 66, 591-610, 10.1007/s10872-010-0049-1, 2010.

652 Hu, Z., Huang, B., Geng, L., and Wang, N.: Sediment provenance in the Northern South China Sea since the Late Miocene,
653 *Open Geosci.*, 14, 454, 10.1515/geo-2022-0454, 2022.

654 Huang, T.-H., Chen, C.-T. A., Bai, Y., and He, X.: Elevated primary productivity triggered by mixing in the quasi-cul-de-sac
655 Taiwan Strait during the NE monsoon, *Sci. Rep.*, 10, 7846, 10.1038/s41598-020-64580-6, 2020.

656 Jagoutz, O., Macdonald, F. A., and Royden, L.: Low-latitude arc–continent collision as a driver for global cooling, *Proc. Nat.*
657 *Acad. Sci.*, 113, 4935-4940, 10.1073/pnas.1523667113, 2016.

658 Jakob, K. A., Wilson, P. A., Pross, J., Ezard, T. H. G., Fiebig, J., Repschläger, J., and Friedrich, O.: A new sea-level record
659 for the Neogene/Quaternary boundary reveals transition to a more stable East Antarctic Ice Sheet, *Proc. Nat. Acad. Sci.*, 117,
660 30980-30987, doi:10.1073/pnas.2004209117, 2020.

661 Janapati, J., Seela, B. K., Lin, P.-L., Wang, P. K., and Kumar, U.: An assessment of tropical cyclones rainfall erosivity for
662 Taiwan, *Sci. Rep.*, 9, 15862, 10.1038/s41598-019-52028-5, 2019.

663 Jin, L., Shan, X., Vaucher, R., Qiao, S., Wang, C., Liu, S., Wang, H., Fang, X., Bai, Y., Zhu, A., and Shi, X.: Sea-level
664 changes control coastal organic carbon burial in the East China Sea during the late MIS 3, *Earth Planet. Sci. Lett.*, 229,
665 104225, 10.1016/j.gloplacha.2023.104225, 2023.

666 Kämpf, N. and Schwertmann, U.: Goethite and hematite in a climosequence in southern Brazil and their application in
667 classification of kaolinitic soils, *Geoderma*, 29, 27-39, 10.1016/0016-7061(83)90028-9, 1983.

668 Kao, S.-J., Shiah, F.-K., Wang, C.-H., and Liu, K.-K.: Efficient trapping of organic carbon in sediments on the continental
669 margin with high fluvial sediment input off southwestern Taiwan, *Cont. Shelf Res.*, 26, 2520-2537,
670 10.1016/j.csr.2006.07.030, 2006.

671 Kao, S. J. and Milliman, J. D.: Water and sediment discharge from small mountainous rivers, Taiwan: The roles of lithology,
672 episodic events, and human activities, *J. Geol.*, 116, 431-448, 10.1086/590921, 2008.

673 Kissel, C., Liu, Z., Li, J., and Wandres, C.: Magnetic minerals in three Asian rivers draining into the South China Sea: Pearl,
674 Red, and Mekong Rivers, *Geochem. Geophys. Geosyst.*, 17, 1678-1693, 10.1002/2016GC006283, 2016.

675 Kissel, C., Liu, Z., Li, J., and Wandres, C.: Magnetic signature of river sediments drained into the southern and eastern part
676 of the South China Sea (Malay Peninsula, Sumatra, Borneo, Luzon and Taiwan), *Sediment. Geol.*, 347, 10-20,
677 10.1016/j.sedgeo.2016.11.007, 2017.

678 Krumins, V., Gehlen, M., Arndt, S., Van Cappellen, P., and Regnier, P.: Dissolved inorganic carbon and alkalinity fluxes
679 from coastal marine sediments: model estimates for different shelf environments and sensitivity to global change,
680 *Biogeosciences*, 10, 371-398, 10.5194/bg-10-371-2013, 2013.

681 Lee, T.-Y., Huang, J.-C., Lee, J.-Y., Jien, S.-H., Zehetner, F., and Kao, S.-J.: Magnified sediment export of small
682 mountainous rivers in Taiwan: Chain reactions from increased rainfall intensity under global warming, *PLoS One*, 10,
683 e0138283, 10.1371/journal.pone.0138283, 2015.

684 Li, B., Wang, J., Huang, B., Li, Q., Jian, Z., Zhao, Q., Su, X., and Wang, P.: South China Sea surface water evolution over
685 the last 12 Myr: A south-north comparison from Ocean Drilling Program Sites 1143 and 1146, *Paleoceanography*, 19,
686 PA1009, 10.1029/2003PA000906, 2004.

687 Li, L., Li, Q., Tian, J., Wang, P., Wang, H., and Liu, Z.: A 4-Ma record of thermal evolution in the tropical western Pacific
688 and its implications on climate change, *Earth Planet. Sci. Lett.*, 309, 10-20, 10.1016/j.epsl.2011.04.016, 2011.

689 Li, M., Wan, S., Colin, C., Jin, H., Zhao, D., Pei, W., Jiao, W., Tang, Y., Tan, Y., Shi, X., and Li, A.: Expansion of C4 plants
690 in South China and evolution of East Asian monsoon since 35 Ma: Black carbon records in the northern South China Sea,
691 *Global Planet. Change*, 223, 104079, 10.1016/j.gloplacha.2023.104079, 2023.

692 Li, X.-h., Wei, G., Shao, L., Liu, Y., Liang, X., Jian, Z., Sun, M., and Wang, P.: Geochemical and Nd isotopic variations in
693 sediments of the South China Sea: a response to Cenozoic tectonism in SE Asia, *Earth Planet. Sci. Lett.*, 211, 207-220,
694 10.1016/S0012-821X(03)00229-2, 2003.

695 Lin, A. T.-S. and Watts, A. B.: Origin of the West Taiwan basin by orogenic loading and flexure of a rifted continental
696 margin, *Journal of Geophysical Research: Solid Earth*, 107, ETG 2-1-ETG 2-19, 10.1029/2001jb000669, 2002.

697 Lin, H.-T., Yang, J.-I., Wu, Y.-T., Shiau, Y.-J., Lo, L., and Yang, S.-H.: The spatiotemporal variations of marine nematode
698 populations may serve as indicators of changes in marine ecosystems, *Mar. Pollut. Bull.*, 211, 117373,
699 10.1016/j.marpolbul.2024.117373, 2025.

700 Lisiecki, L. E. and Raymo, M. E.: A Pliocene-Pleistocene stack of 57 globally distributed benthic $\delta^{18}\text{O}$ records,
701 *Paleoceanography*, 20, PA1003, 10.1029/2004pa001071, 2005.

702 Liu, J., Chen, Z., Chen, M., Yan, W., Xiang, R., and Tang, X.: Magnetic susceptibility variations and provenance of surface
703 sediments in the South China Sea, *Sediment. Geol.*, 230, 77-85, 10.1016/j.sedgeo.2010.07.001, 2010a.

704 Liu, J. P., Liu, C. S., Xu, K. H., Milliman, J. D., Chiu, J. K., Kao, S. J., and Lin, S. W.: Flux and fate of small mountainous
705 rivers derived sediments into the Taiwan Strait, *Mar. Geol.*, 256, 65-76, 10.1016/j.margeo.2008.09.007, 2008.

706 Liu, J. P., Xue, Z., Ross, K., Wang, H. J., Yang, Z. S., Li, A. C., and Gao, S.: Fate of sediments delivered to the sea by Asian
707 large rivers: Long-distance transport and formation of remote alongshore clinotherms, *Sed. Record*, 7, 4-9, 10.2110/
708 sedred.2009.4.4, 2009a.

709 Liu, J. T., Kao, S. J., Huh, C. A., and Hung, C. C.: Gravity flows associated with flood events and carbon burial: Taiwan as
710 instructional source area, *Annu. Rev. Mar. Sci.*, 5, 47-68, 10.1146/annurev-marine-121211-172307, 2013.

711 Liu, J. T., Wang, Y.-H., Yang, R. J., Hsu, R. T., Kao, S.-J., Lin, H.-L., and Kuo, F. H.: Cyclone-induced hyperpycnal
712 turbidity currents in a submarine canyon, *J. Geophys. Res. [Oceans]*, 117, C04033, 10.1029/2011jc007630, 2012.

713 Liu, J. T., Hung, J.-J., Lin, H.-L., Huh, C.-A., Lee, C.-L., Hsu, R. T., Huang, Y.-W., and Chu, J. C.: From suspended
714 particles to strata: The fate of terrestrial substances in the Gaoping (Kaoping) submarine canyon, *J. Mar. Syst.*, 76, 417-432,
715 10.1016/j.jmarsys.2008.01.010, 2009b.

716 Liu, Z., Alain, T., Clemens, S. C., and Wang, P.: Quaternary clay mineralogy in the northern South China Sea (ODP Site
717 1146), *Science in China Series D: Earth Sciences*, 46, 1223-1235, 10.1360/02yd0107, 2003.

718 Liu, Z., Zhao, Y., Colin, C., Siringan, F. P., and Wu, Q.: Chemical weathering in Luzon, Philippines from clay mineralogy
719 and major-element geochemistry of river sediments, *Appl. Geochem.*, 24, 2195-2205, 10.1016/j.apgeochem.2009.09.025,
720 2009c.

721 Liu, Z., Colin, C., Huang, W., Le, K. P., Tong, S., Chen, Z., and Trentesaux, A.: Climatic and tectonic controls on
722 weathering in south China and Indochina Peninsula: Clay mineralogical and geochemical investigations from the Pearl, Red,
723 and Mekong drainage basins, *Geochem. Geophys. Geosyst.*, 8, Q05005, 10.1029/2006gc001490, 2007.

724 Liu, Z., Colin, C., Li, X., Zhao, Y., Tuo, S., Chen, Z., Siringan, F. P., Liu, J. T., Huang, C.-Y., You, C.-F., and Huang, K.-F.:
725 Clay mineral distribution in surface sediments of the northeastern South China Sea and surrounding fluvial drainage basins:
726 Source and transport, *Mar. Geol.*, 277, 48-60, 10.1016/j.margeo.2010.08.010, 2010b.

727 Liu, Z., Zhao, Y., Colin, C., Stattegger, K., Wiesner, M. G., Huh, C.-A., Zhang, Y., Li, X., Sompongchaiyakul, P., You, C.-
728 F., Huang, C.-Y., Liu, J. T., Siringan, F. P., Le, K. P., Sathiamurthy, E., Hantoro, W. S., Liu, J., Tuo, S., Zhao, S., Zhou, S.,
729 He, Z., Wang, Y., Bunsomboonsakul, S., and Li, Y.: Source-to-sink transport processes of fluvial sediments in the South
730 China Sea, *Earth Sci. Rev.*, 153, 238-273, 10.1016/j.earscirev.2015.08.005, 2016.

731 Lüdmann, T., Wong, H. K., and Berglar, K.: Upward flow of North Pacific Deep Water in the northern South China Sea as
732 deduced from the occurrence of drift sediments, *Geophys. Res. Lett.*, 32, 1-4, 10.1029/2004GL021967, 2005.

733 Luo, X., Zhou, H., Satriawan, T. W., Tian, J., Zhao, R., Keenan, T. F., Griffith, D. M., Sitch, S., Smith, N. G., and Still, C.
734 J.: Mapping the global distribution of C4 vegetation using observations and optimality theory, *Nat. Commun.*, 15, 1219,
735 10.1038/s41467-024-45606-3, 2024.

736 Lurcock, P. C. and Wilson, G. S.: PuffinPlot: A versatile, user-friendly program for paleomagnetic analysis, *Geochem.*
737 *Geophys. Geosyst.*, 13, Q06Z45, 10.1029/2012GC004098, 2012.

738 Macdonald, F. A., Swanson-Hysell, N. L., Park, Y., Lisiecki, L., and Jagoutz, O.: Arc-continent collisions in the tropics set
739 Earth's climate state, *Science*, 364, 181-184, 10.1126/science.aav5300, 2019.

740 Maher, B. A.: Characterisation of soils by mineral magnetic measurements, *Phys. Earth Planet. Inter.*, 42, 76-92,
741 10.1016/S0031-9201(86)8010-3, 1986.

742 Martiny, A. C., Pham, C. T. A., Primeau, F. W., Vrugt, J. A., Moore, J. K., Levin, S. A., and Lomas, M. W.: Strong
743 latitudinal patterns in the elemental ratios of marine plankton and organic matter, *Nat. Geosci.*, 6, 279-283,
744 10.1038/ngeo1757, 2013.

745 Miller, K. G., Browning, J. V., Schmelz, W. J., Kopp, R. E., Mountain, G. S., and Wright, J. D.: Cenozoic sea-level and
746 cryospheric evolution from deep-sea geochemical and continental margin records, *Sci. Adv.*, 6, eaaz1346,
747 10.1126/sciadv.aaz1346, 2020.

748 Milliman, J. D. and Kao, S.-J.: Hyperpycnal discharge of fluvial sediment to the ocean: Impact of super-typhoon Herb
749 (1996) on Taiwanese rivers, *J. Geol.*, 113, 503-516, 10.1086/431906, 2005.

750 Milliman, J. D. and Syvitski, J. P. M.: Geomorphic/tectonic control of sediment discharge to the ocean: The importance of
751 small mountainous rivers, *J. Geol.*, 100, 525-544, 10.1086/629606, 1992.

752 Milliman, J. D., Lee, T. Y., Huang, J. C., and Kao, S. J.: Impact of catastrophic events on small mountainous rivers:
753 Temporal and spatial variations in suspended- and dissolved-solid fluxes along the Choshui River, central western Taiwan,
754 during typhoon Mindulle, July 2–6, 2004, *Geochim. Cosmochim. Acta*, 205, 272-294, 10.1016/j.gca.2017.02.015, 2017.

755 Nagel, S., Granjeon, D., Willett, S., Lin, A. T.-S., and Castelltort, S.: Stratigraphic modeling of the Western Taiwan foreland
756 basin: Sediment flux from a growing mountain range and tectonic implications, *Mar. Pet. Geol.*, 96, 331-347,
757 10.1016/j.marpetgeo.2018.05.034, 2018.

758 Nagel, S., Castelltort, S., Wetzel, A., Willett, S. D., Mouthereau, F., and Lin, A. T.: Sedimentology and foreland basin
759 paleogeography during Taiwan arc continent collision, *J. Asian Earth Sci.*, 62, 180-204, 10.1016/j.jseaes.2012.09.001, 2013.

760 Nie, J., Stevens, T., Song, Y., King, J. W., Zhang, R., Ji, S., Gong, L., and Cares, D.: Pacific freshening drives Pliocene
761 cooling and Asian monsoon intensification, *Sci. Rep.*, 4, 5474, 10.1038/srep05474, 2014.

762 Pan, T.-Y., Lin, A. T.-S., and Chi, W.-R.: Paleoenvironments of the evolving Pliocene to early Pleistocene foreland basin in
763 northwestern Taiwan: An example from the Dahan River section, *Isl. Arc*, 24, 317-341, 10.1111/iar.12113, 2015.

764 Peterson, B. J. and Fry, B.: Stable isotopes in ecosystem studies, *Annu. Rev. Ecol. Evol. Syst.*, 18, 293-320,
765 10.1146/annurev.es.18.110187.001453, 1987.

766 Raymo, M. E. and Ruddiman, W. F.: Tectonic forcing of late Cenozoic climate, *Nature*, 359, 117-122, 10.1038/359117a0,
767 1992.

768 Robinson, M. M., Dowsett, H. J., and Chandler, M. A.: Pliocene role in assessing future climate impacts, *Eos*, 89, 501-502,
769 10.1029/2008EO490001, 2008.

770 Rohling, E. J., Foster, G. L., Grant, K. M., Marino, G., Roberts, A. P., Tamisiea, M. E., and Williams, F.: Sea-level and
771 deep-sea-temperature variability over the past 5.3 million years, *Nature*, 508, 477-482, 10.1038/nature13230, 2014.

772 Schlumberger: Log Interpretation Principles/Applications, Schlumberger, Houston, 233 pp.1989.

773 Shao, L., Li, X., Wei, G., Liu, Y., and Fang, D.: Provenance of a prominent sediment drift on the northern slope of the South
774 China Sea, *Science in China Series D: Earth Sciences*, 44, 919-925, 10.1007/BF02907084, 2001.

775 Shao, L., Qiao, P.-J., Pang, X., Wei, G.-J., Li, Q.-Y., Miao, W.-L., and Li, A.: Nd isotopic variations and its implications in
776 the recent sediments from the northern South China Sea, *Chin. Sci. Bull.*, 54, 311-317, 10.1007/s11434-008-0453-8, 2009.

777 Shea, K.-S. and Huang, T.: Tertiary stratigraphy in Taiwan, *The Taiwan Mining Industry*, 55, 17-32, 2003.

778 Shih, Y.-Y., Lin, H.-H., Li, D., Hsieh, H.-H., Hung, C.-C., and Chen, C.-T. A.: Elevated carbon flux in deep waters of the
779 South China Sea, *Sci. Rep.*, 9, 1496, 10.1038/s41598-018-37726-w, 2019.

780 Spangenberg, J. E.: Bulk C, H, O, and fatty acid C stable isotope analyses for purity assessment of vegetable oils from the
781 southern and northern hemispheres, *Rapid Commun. Mass Spectrom.*, 30, 2447-2461, 10.1002/rcm.7734, 2016.

782 Stepanauskas, R., JØrgensen, N. O. G., Eigaard, O. R., Žvikas, A., Tranvik, L. J., and Leonardson, L.: Summer inputs of
783 riverine nutrients to the Baltic Sea: Bioavailability and eutrophication relevance, *Ecol. Monogr.*, 72, 579-597, 10.1890/0012-
784 9615(2002)072[0579:SIORNT]2.0.CO;2, 2002.

785 Still, C., Berry, J., Collatz, G., and Defries, R.: Global distribution of C3 and C4 vegetation: Carbon cycle implications,
786 *Global Biogeochem. Cycles*, 17, 6-1, 10.1029/2001GB001807, 2003.

787 Teng, L. S., Wang, Y., Tang, C.-H., Huang, C.-Y., Huang, T.-C., Yu, M.-S., and Ke, A.: Tectonic aspects of the Paleogene
788 depositional basin of northern Taiwan, *Proc. Geol. Soc. China*, 34, 313-336, 1991.

789 Thunell, R. C., Qingmin, M., Calvert, S. E., and Pedersen, T. F.: Glacial-Holocene Biogenic Sedimentation Patterns in the
790 South China Sea: Productivity Variations and Surface Water pCO₂, *Paleoceanography*, 7, 143-162, 10.1029/92PA00278,
791 1992.

792 Tian, J., Wang, P., Cheng, X., and Li, Q.: Establishment of the Plio-Pleistocene astronomical timescale of ODP site 1143,
793 Southern South China Sea, *Journal of China University of Geosciences*, 30, 31-39, 2005.

794 Tian, J., Xie, X., Ma, W., Jin, H., and Wang, P.: X-ray fluorescence core scanning records of chemical weathering and
795 monsoon evolution over the past 5 Myr in the southern South China Sea, *Paleoceanography*, 26, 10.1029/2010PA002045,
796 2011.

797 Tian, J., Zhao, Q., Wang, P., Li, Q., and Cheng, X.: Astronomically modulated Neogene sediment records from the South
798 China Sea, *Paleoceanography*, 23, 10.1029/2007PA001552, 2008.

799 Tierney, J. E., Haywood, A. M., Feng, R., Bhattacharya, T., and Otto-Bliesner, B. L.: Pliocene warmth consistent with
800 greenhouse gas forcing, *Geophys. Res. Lett.*, 46, 9136-9144, 10.1029/2019gl083802, 2019.

801 Tory, K. J. and Frank, W. M.: Tropical Cyclone Formation, in: *Global Perspectives on Tropical Cyclones*, 55-91,
802 10.1142/9789814293488_0002, 2010.

803 Van Oost, K., Verstraeten, G., Doetterl, S., Notebaert, B., Wiaux, F., Broothaerts, N., and Six, J.: Legacy of human-induced
804 C erosion and burial on soil–atmosphere C exchange, *Proc. Nat. Acad. Sci.*, 109, 19492–19497, 10.1073/pnas.1211162109,
805 2012.

806 Vaucher, R., Dillinger, A., Hsieh, A. I., Chi, W.-R., Löwemark, L., and Dashtgard, S. E.: Storm-flood-dominated delta
807 succession in the Pleistocene Taiwan Strait, *The Depositional Record*, 00, 1–24, 10.1002/dep2.231, 2023a.

808 Vaucher, R., Zeeden, C., Hsieh, A. I., Kaboth-Bahr, S., Lin, A. T., Horng, C.-S., and Dashtgard, S. E.: Hydroclimate
809 dynamics during the Plio-Pleistocene transition in the northwest Pacific realm, *Global Planet. Change*, 223, 104088,
810 10.1016/j.gloplacha.2023.104088, 2023b.

811 Vaucher, R., Dashtgard, S. E., Horng, C. S., Zeeden, C., Dillinger, A., Pan, Y. Y., Setiaji, R. A., Chi, W. R., and Lowemark,
812 L.: Insolation-paced sea level and sediment flux during the early Pleistocene in Southeast Asia, *Sci. Rep.*, 11, 16707,
813 10.1038/s41598-021-96372-x, 2021.

814 Walker, J. C. G., Hays, P. B., and Kasting, J. F.: A negative feedback mechanism for the long-term stabilization of Earth's
815 surface temperature, *J. Geophys. Res. [Oceans]*, 86, 9776–9782, 10.1029/JC086iC10p09776, 1981.

816 Wan, S., Li, A., Clift, P. D., and Jiang, H.: Development of the East Asian summer monsoon: Evidence from the sediment
817 record in the South China Sea since 8.5 Ma, *Palaeogeogr. Palaeoclimatol. Palaeoecol.*, 241, 139–159,
818 10.1016/j.palaeo.2006.06.013, 2006.

819 Wan, S., Li, A., Clift, P. D., and Stuut, J.-B. W.: Development of the East Asian monsoon: Mineralogical and
820 sedimentologic records in the northern South China Sea since 20 Ma, *Palaeogeogr. Palaeoclimatol. Palaeoecol.*, 254, 561–
821 582, 10.1016/j.palaeo.2007.07.009, 2007a.

822 Wan, S., Clift, P. D., Li, A., Li, T., and Yin, X.: Geochemical records in the South China Sea: implications for East Asian
823 summer monsoon evolution over the last 20 Ma, *Geol. Soc. Lond. Spec. Pub.*, 342, 245–263, doi:10.1144/SP342.14, 2010a.

824 Wan, S., Tian, J., Steinke, S., Li, A., and Li, T.: Evolution and variability of the East Asian summer monsoon during the
825 Pliocene: Evidence from clay mineral records of the South China Sea, *Palaeogeogr. Palaeoclimatol. Palaeoecol.*, 293, 237–
826 247, 10.1016/j.palaeo.2010.05.025, 2010b.

827 Wan, S., Li, A., Clift, P. D., Wu, S., Xu, K., and Li, T.: Increased contribution of terrigenous supply from Taiwan to the
828 northern South China Sea since 3 Ma, *Mar. Geol.*, 278, 115–121, 10.1016/j.margeo.2010.09.008, 2010c.

829 Wan, S. M., Li, A. C., Jan-Berend, W. S., and Xu, F. J.: Grain-size records at ODP site 1146 from the northern South China
830 Sea: Implications on the East Asian monsoon evolution since 20 Ma, *Science in China Series D: Earth Sciences*, 50, 1536–
831 1547, 10.1007/s11430-007-0082-0, 2007b.

832 Wang, H., Lu, H., Zhao, L., Zhang, H., Lei, F., and Wang, Y.: Asian monsoon rainfall variation during the Pliocene forced
833 by global temperature change, *Nat. Commun.*, 10, 5272, 10.1038/s41467-019-13338-4, 2019.

834 Wang, P., Prell, W. L., Blum, P., and Party, S. S.: Site 1148, 1–121, 10.2973/odp.proc.ir.184.109.2000, 2000a.

835 Wang, P., Prell, W. L., Blum, P., and Party, S. S.: Site 1146, 1–101, doi:10.2973/odp.proc.ir.184.108.2000, 2000b.

836 Wang, P., Prell, W. L., Blum, P., and Shipboard Scientific, P.: Magnetic susceptibility on ODP Hole 184-1146C,
837 PANGAEA [dataset], 10.1594/PANGAEA.266354, 2005a.

838 Wang, P., Clemens, S., Beaufort, L., Braconnot, P., Ganssen, G., Jian, Z., Kershaw, P., and Sarnthein, M.: Evolution and
839 variability of the Asian monsoon system: state of the art and outstanding issues, *Quat. Sci. Rev.*, 24, 595-629,
840 10.1016/j.quascirev.2004.10.002, 2005b.

841 Wang, R. and Ma, L.: Climate-driven C4 plant distributions in China: divergence in C4 taxa, *Sci. Rep.*, 6, 27977,
842 10.1038/srep27977, 2016.

843 Westerhold, T., Marwan, N., Drury, A. J., Liebrand, D., Agnini, C., Anagnostou, E., Barnet, J. S. K., Bohaty, S. M., De
844 Vleeschouwer, D., Florindo, F., Frederichs, T., Hodell, D. A., Holbourn, A. E., Kroon, D., Lauretano, V., Littler, K.,
845 Lourens, L. J., Lyle, M., Pälike, H., Röhl, U., Tian, J., Wilkens, R. H., Wilson, P. A., and Zachos, J. C.: An astronomically
846 dated record of Earth's climate and its predictability over the last 66 million years, *Science*, 369, 1383-1388,
847 10.1126/science.aba6853, 2020.

848 Wilkens, R. H., Westerhold, T., Drury, A. J., Lyle, M., Gorgas, T., and Tian, J.: Revisiting the Ceara Rise, equatorial
849 Atlantic Ocean: isotope stratigraphy of ODP Leg 154 from 0 to 5 Ma, *Clim. Past*, 13, 779-793, 10.5194/cp-13-779-2017,
850 2017.

851 Xin, S., Shen, J., Zhang, W., Sun, W., and Xiao, X.: East Asian winter monsoon evolution since the late Pliocene based on a
852 pollen record from Lake Xingkai, northeast Asia, *Quat. Res.*, 93, 40-59, 10.1017/qua.2019.45, 2020.

853 Xue, J., Chen, J., Li, Y., Huo, J., Zhao, Z., Liu, Y., and Chen, M.: Expansion of C4 plants in the tropical Leizhou Peninsula
854 during the Last Glacial Maximum: Modulating effect of regional sea-level change, *Sci. Tot. Environ.*, 952, 175897,
855 10.1016/j.scitotenv.2024.175897, 2024.

856 Yan, Q., Zhang, Z., and Zhang, R.: Investigating sensitivity of East Asian monsoon to orbital forcing during the late Pliocene
857 Warm Period, *J. Geophys. Res. [Atmos.]*, 10.1029/2017jd027646, 2018.

858 Yan, Q., Wei, T., Zhang, Z., and Jiang, N.: Orbitally induced variation of tropical cyclone genesis potential over the western
859 North Pacific during the mid-Piacenzian Warm Period: A modeling perspective, *Paleoceanogr. Paleoclimatol.*, 34, 902-916,
860 10.1029/2018pa003535, 2019.

861 Yan, Q., Wei, T., Korty, R. L., Kossin, J. P., Zhang, Z., and Wang, H.: Enhanced intensity of global tropical cyclones during
862 the mid-Pliocene warm period, *Proc. Nat. Acad. Sci.*, 113, 12963-12967, 10.1073/pnas.1608950113, 2016.

863 Yang, S., Ding, Z., Feng, S., Jiang, W., Huang, X., and Guo, L.: A strengthened East Asian Summer Monsoon during
864 Pliocene warmth: Evidence from 'red clay' sediments at Pianguan, northern China, *J. Asian Earth Sci.*, 155, 124-133,
865 10.1016/j.jseaes.2017.10.020, 2018.

866 Yin, S., Hernández-Molina, F. J., Lin, L., He, M., Gao, J., and Li, J.: Plate convergence controls long-term full-depth
867 circulation of the South China Sea, *Mar. Geol.*, 459, 107050, 10.1016/j.margeo.2023.107050, 2023.

868 Yu, H.-S., Chiang, C.-S., and Shen, S.-M.: Tectonically active sediment dispersal system in SW Taiwan margin with
869 emphasis on the Gaoping (Kaoping) Submarine Canyon, *J. Mar. Syst.*, 76, 369-382, 10.1016/j.jmarsys.2007.07.010, 2009.

870 Zhang, Y., Liu, Z., Zhao, Y., Wang, W., Li, J., and Xu, J.: Mesoscale eddies transport deep-sea sediments, *Sci. Rep.*, 4,
871 5937-5937, 10.1038/srep05937, 2014.

872 Zhang, Y. G., Ji, J., Balsam, W., Liu, L., and Chen, J.: Mid-Pliocene Asian monsoon intensification and the onset of
873 Northern Hemisphere glaciation, *Geology*, 37, 599-602, 10.1130/g25670a.1, 2009.

874 Zhao, Y., Liu, Z., Zhang, Y., Li, J., Wang, M., Wang, W., and Xu, J.: In situ observation of contour currents in the northern
875 South China Sea: Applications for deepwater sediment transport, *Earth Planet. Sci. Lett.*, 430, 477-485,
876 10.1016/j.epsl.2015.09.008, 2015.

877 Zheng, L.-W., Ding, X., Liu, J. T., Li, D., Lee, T.-Y., Zheng, X., Zheng, Z., Xu, M. N., Dai, M., and Kao, S.-J.: Isotopic
878 evidence for the influence of typhoons and submarine canyons on the sourcing and transport behavior of biospheric organic
879 carbon to the deep sea, *Earth Planet. Sci. Lett.*, 465, 103-111, 10.1016/j.epsl.2017.02.037, 2017.

880